A Numerical Simulation of Cyclic Mesocyclogenesis

EDWIN J. ADLERMAN AND KELVIN K. DROEGEMEIER

School of Meteorology and Center for Analysis and Prediction of Storms, University of Oklahoma, Norman, Oklahoma

ROBERT DAVIES-JONES

NOAA/National Severe Storms Laboratory, Norman, Oklahoma.

(Manuscript received 4 March 1998, in final form 5 August 1998)

ABSTRACT

A three-dimensional nonhydrostatic numerical model, the Advanced Regional Prediction System, is used to study the process of cyclic mesocyclogenesis in a classic supercell thunderstorm. During the 4-h simulation, the storm's mesocyclone undergoes two distinct occlusions, with the beginning of a third indicated at the end of the simulation. The occlusion process exhibits a period of approximately 60 min and is qualitatively similar in each case.

Initial midlevel (3–7 km) mesocyclogenesis proceeds according to the ''classic'' picture, that is, via tilting of streamwise environmental vorticity. The development of an evaporatively driven rear-flank downdraft (RFD) signals the beginning of the occlusion process. The developing RFD wraps cyclonically around the mesocyclone, causing the gust front to surge outward. Simultaneously, the occluding mesocyclone rapidly intensifies near the surface. Trajectory analyses demonstrate that this intensification follows from the tilting and stretching of near-ground ($<$500 m) streamwise vorticity produced by baroclinic generation, crosswise exchange, and streamwise stretching along descending parcel trajectories in the RFD. The surging gust front also initiates updraft development on the downshear flank at midlevels, resulting in a two-celled updraft structure. As the near-ground mesocyclone becomes detached from the gust front due to the developing occlusion downdraft, the upshear updraft flank weakens as its conditionally unstable inflow is cut off at low levels; at the same time, the downshear updraft flank continues to develop eastward. The end of the occlusion process is signaled as the old near-ground mesocyclone becomes completely embedded near the surface in divergent outflow beneath the decaying updraft and is advected away by the mean flow.

Near-ground mesocyclogenesis is initiated in the new updraft in a process nearly identical to that of the initial mesocyclone. However, after the first occlusion, near-ground equivalent potential temperature and buoyancy contours are fortuitously oriented such that streamwise baroclinic generation can proceed without delay. Thus, although the initial occlusion requires two hours to become fully organized, the second occurs only one hour later. In effect, the occlusion appears to set the stage for more rapid development of subsequent mesocyclones.

1. Introduction

The presence of a deep persistent mesocyclone (i.e., a 3–9-km diameter region of vertical vorticity >0.01 s^{-1} with both height and time continuity) is often chosen as the defining characteristic of a supercell thunderstorm (Doswell and Burgess 1993). Based on earlier work by Lilly (1982, 1983), Davies-Jones (1984) demonstrated using linear theory that the tilting of storm-relative environmental streamwise vorticity by an updraft can account for initial *midlevel* mesocyclogenesis in any generalized wind profile. Both observational and numerical studies (e.g., Lilly 1982, 1983, 1986a,b; Rotunno and Klemp 1982; Weisman and Klemp 1982; Klemp and Rotunno 1983; Brandes 1984; Rotunno and Klemp 1985; Davies-Jones et al. 1990; Droegemeier et al. 1993) support this hypothesis.

The development of *low-level* rotation in a homogeneous environment cannot proceed similarly since environmental streamlines and barotropic vortex lines cannot turn sharply upward near the ground (Davies-Jones 1982; Davies-Jones and Brooks 1993; Davies-Jones 1996) in the absence of strong upward pressure-gradient forces, such as those generated by a dynamic-pipe effect (Leslie 1971; Trapp and Davies-Jones 1997) or at the head of a gust front (e.g., Simpson 1972). Since the large-scale mesocyclone circulation never attains cyclostrophic balance and therefore remains porous to radial parcel motions, it is unlikely that the dynamic-pipe effect is important for the initial development of rotation near the ground. Near-ground ($<$500 m) mesocyclogenesis in the cool air just behind the gust front therefore must evolve as a result of the reorientation of baroclinic

Corresponding author address: Mr. Edwin Adlerman, School of Meteorology, University of Oklahoma, 100 E. Boyd St., Rm 1310, Norman OK 73019.
E-mail: eadlerman@ou.edu

vortex lines—generated by buoyancy gradients—by the updraft (Klemp and Rotunno 1983; Rotunno and Klemp 1985) and both the downdraft and updraft (Davies-Jones and Brooks 1993; Brooks et al. 1993; Brooks et al. 1994; Wicker and Wilhelmson 1995; Davies-Jones 1996).

Although our understanding of mesocyclone dynamics has advanced significantly in the last 15 years, the corresponding process whereby one supercell can produce a periodic succession of low and/or midlevel mesocyclones, that is, ''cyclic mesocyclogenesis,'' remains relatively uninvestigated. In this study, we use a numerical simulation to investigate cyclic mesocyclogenesis, with emphasis on the dynamics of the process itself.

The phenomenon of cyclic mesocyclogenesis was first observed well before the dynamics of severe storms became quantified through numerical modeling and theory (e.g., Hoecker 1959). Darkow and Roos (1970) studied Missouri tornadoes and observed that approximately 20% of the associated thunderstorms produced multiple tornadoes at intervals ranging from 20 min to 2 h, with a mean period of approximately 45 min. Observations from the Palm Sunday tornado outbreak of 11 April 1965 (Fujita et al. 1970) and the 3 April 1974 ''superoutbreak'' (Fujita 1975; Forbes 1975, 1977) emphasized the dominance of cyclic-type supercells in certain environments. Early explanations of this phenomenon included the presence of multiple tornadoes rotating around a single mesocyclone (Snow and Agee 1975; Agee et al. 1976), thereby producing the familiar cycloidal damage paths associated with tornado families (e.g., Forbes 1975).

Lemon and Doswell (1979) used radar, aircraft, and visual observations to develop a conceptual model of mesocyclone/updraft evolution. They suggested that cyclic tornadogenesis results from the development of a *new* updraft/mesocyclone following the occlusion of the initial updraft/mesocyclone. This hypothesis was later supported both by field observations (e.g., Rasmussen et al. 1982; Jensen et al. 1983) and by a comprehensive survey by Burgess et al. (1982) of National Severe Storms Laboratory single–Doppler radar archives from 1971–77. The latter study observed that most (76%) mesocyclones consist of a single core during their lifetime (a core being defined as an area of solid-body rotation within a broader region of cyclonic motion on the order of 20 km). The remaining cases consisted of multiple cores, forming and dissipating through a cyclic occlusion process with a period of approximately 40 min (Fig. 1).

Moller et al. (1994) observed that most major tornado outbreaks are composed of classic supercells. However, it is important to note that recent research suggests a continuum of severe storms that extends not only through the low-precipitation (LP) to high-precipitation (HP) spectrum (Doswell and Burgess 1993), but also includes such phenomenon as hybrid storms (Foote and Frank 1983; Nelson 1987), transitional storms (Vasiloff et al. 1986; Richardson and Droegemeier 1996; Richardson et al. 1998), and shallow-topped supercells in hurricane and other environments (McCaul 1991, 1993;

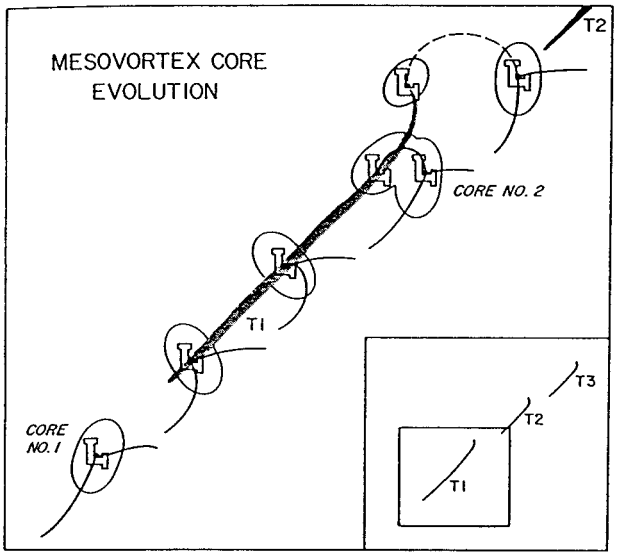

FIG. 1. Conceptual model of mesocyclone core evolution as proposed by Burgess et al. (1982). Dark shaded lines indicate tornado tracks, and thin lines represent low-level wind discontinuities (gust front).

Foster et al. 1994; Monteverdi and Quadros 1994; McCaul and Weisman 1996; Wicker and Cantrell 1996). Consequently, it is likely that a continuum of cyclic-type supercells also exists, and this study may not be applicable to all cases. Indeed, a recent study by Kulie and Lin (1998) supports such a conclusion. Using a numerical model, they demonstrate a unique mode of cyclic low-level mesocyclogenesis in a hybrid HP tornadic supercell, which lacks a midlevel mesocyclone throughout its lifetime.

Brandes (1993) points out that the entire dual-Doppler archive of well-sampled supercell thunderstorms is limited to only approximately 10 cases. Comprehensive dual-Doppler observations of cyclic mesocyclogenesis are even more limited (Dowell et al. 1997) and the use of a numerical model is therefore warranted. The objective of this study is to investigate the process of cyclic mesocyclogenesis in a ''classic'' supercell thunderstorm through the use of an idealized three-dimensional storm-scale numerical simulation. We focus primarily on 1) the physical mechanisms responsible for initial mesocyclogenesis, 2) the evolution of the occlusion process and the importance of the rear-flank downdraft, and 3) the process of updraft redevelopment and mesocyclogenesis associated with subsequent cycles. Since the development of near-ground rotation is still a matter of debate (e.g., Wicker and Wilhelmson 1995), a trajectory analysis is also presented in the context of a full three-dimensional vorticity decomposition in seminatural coordinates. Although streamwise baroclinic generation along parcel paths is shown to be a secondary effect for near-ground mesocyclogenesis, it nonetheless plays a role in explaining the rapidity by which subsequent mesocyclones form after the first occlusion. From this anal-

TABLE 1. Physical and computational parameters used in the numerical simulation.

Parameter	Symbol	Value
Horizontal resolution	Δx, Δy	500 m
Vertical resolution	Δz	100 m $\leq \Delta z \leq$ 700 m
Large time step	Δt	3.75 s
Small time step	$\Delta \tau$	0.75 s
Coriolis parameter	f	0.0 s^{-1}
Nondimensional surface drag coefficient	C_d	0.0
Turbulent Prandtl number	K_m/K_h	0.471
Fourth-order horizontal mixing coefficient	K_4	6.25×10^7 m^4 s^{-1}
Second-order vertical mixing coefficient	K_2	$1.5 \leq K_2 \leq 73.5$ m^2 s^{-1}
Initial thermal perturbation:		
Magnitude	$\Delta\Theta$	4.0 K
Horizontal radius	x_r, y_r	9 km
Vertical radius	z_r	1.5 km
Height of center above ground	z_c	1.5 km

ysis, a conceptual model of the cycling process is developed and compared with the observations of Lemon and Doswell (1979) and Burgess et al. (1982). We defer to future papers an explanation of those factors that delineate cyclic from noncyclic storms and that govern the behavior (e.g., periodicity) of the cycling process.

The paper is organized as follows. Section 2 discusses the numerical model used in the simulations. Section 3 gives a brief overview of the entire supercell evolution and introduces the five-stage conceptual model of the occlusion process. Section 4 details the simulation results that lead to the conceptual model. Section 5 summarizes the results and discusses their implications.

2. Model description

The simulation described in this study was made using version 4.0 of the Advanced Regional Prediction System, a three-dimensional, compressible, nonhydrostatic model developed for storm-scale weather prediction (Xue et al. 1995). The grid has a uniform horizontal spacing of 500 m within a 100 $\times$ 100 km domain. In the vertical 43 levels are used over a depth of 16 km, with a vertical grid spacing that varies from 100 m near the ground to 700 m near the top of the domain. The stretching function is a hyperbolic tangent, resulting in 14 levels below 2 km. This allows for adequate vertical representation of the low-level storm structure, including the cold outflow and gust front. A radiation condition is used at the lateral boundaries, and the upper and lower boundaries are rigid, with a Rayleigh sponge layer above the tropopause. Cloud microphysics is treated using the Kessler warm-rain parameterization scheme, while subgrid-scale turbulent mixing is represented using 1.5-order turbulent kinetic-energy closure. A minimal amount of explicit diffusion is included to prevent aliasing instability. Divergence damping is also used to help suppress sound waves. The Coriolis force, surface friction, surface physics, and terrain are not included. A summary of model parameters is shown in Table 1.

The homogeneous model base state is initialized using a composited sounding from the well-documented 20 May 1977 Del City, Oklahoma, storm (Ray et al. 1981; Johnson et al. 1987), which has been used in several other modeling studies (Klemp et al. 1981; Klemp and Rotunno 1983; Grasso and Cotton 1995). This sounding is characterized by a convective available potential energy of approximately 2600 J kg^{-1} and a 0–3-km storm-relative environmental helicity (Davies-Jones et al. 1990) of approximately 150 m^2 s^{-2} (Fig. 2). A mean storm motion of $(u, v) = (3, 14)$ m s^{-1} is subtracted to keep the storm relatively stationary and away from the lateral boundaries. An ellipsoidal thermal bubble of amplitude 4 K, horizontal radius 9 km, and maximum vertical depth of 1.5 km is placed 1.5 km above ground level to initiate convection. The model is integrated for 4 h of simulation time. Starting at 1 h, history files are saved every minute in order to facilitate accurate trajectory calculations and other analyses.

3. Simulation overview and conceptual model

The transient development of the initial impulse follows similarly as in other idealized simulations (e.g., Klemp et al. 1981) and will not be discussed in detail. The initial updraft peaks at approximately 1200 s and splits into left- and right-moving cells by 1500 s. The right-moving cell dominates throughout the rest of the simulation, developing into a mature supercell with vorticity below 2 km exceeding mesocyclone criteria (0.01 s^{-1}) by 2400 s. The left mover undergoes successive splitting and moves northwest relative to the mature storm. By 3600 s, the supercell has taken on a steady-state character, with a persistent midlevel (3–7 km) mesocyclone and updrafts greater than 35 m s^{-1}.

In order to characterize the overall structure of the cycling process prior to our more detailed analysis, we show in Fig. 3 the principal stages of storm evolution at the surface ($\sim$0.05 km) and at middle levels ($\sim$4 km). This schematic is based on the actual model simulation, with corresponding model times described below. After the dominant right-moving supercell has taken on a steady-state character, the rear-flank downdraft

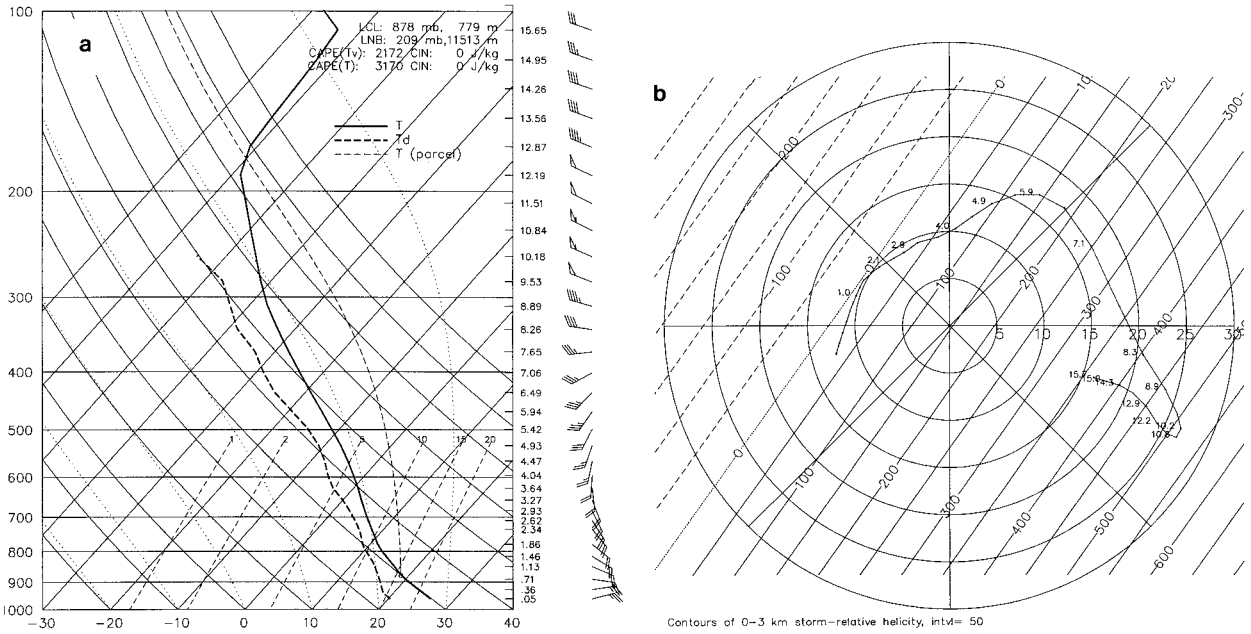

FIG. 2. (a) Sounding and (b) hodograph from the 20 May 1977 Del City, Oklahoma, storm. Both are composited from the 1500 UTC Fort Sill, Oklahoma, and 1620 UTC Elmore City, Oklahoma, soundings, as described in Ray et al. (1981). (b) Circles of constant wind speed are contoured every 5 m s^{-1}, lines of constant 0–3-km storm-relative environmental helicity (for zero storm motion) are labeled every 50 m^2 s^{-2}, and hodograph heights above ground level are labeled in km.

(RFD) intensifies between 3600 and 5200 s and forces the gust front to bow outward (Fig. 3a). Simultaneously, the near-ground (<500 m) mesocyclone intensifies, and vertical vorticity near the ground becomes greater than 0.02 s^{-1}. This is accompanied by a large hook in the rainwater field (Fig. 3b) as precipitation falls in a cyclonic path around the weak-echo region. At midlevels and above (i.e., >3 km), the updraft then takes on a two-cell (i.e., two maxima) structure (Fig. 3b) while the RFD forces the gust front to propagate farther eastward. The near-ground mesocyclone/updraft center occludes (Fig. 3c) and vertical vorticity near the surface rapidly increase to values greater than 0.05 s^{-1}. Between 7200 and 8100 s, the old updraft and corresponding mesocyclone separate from the continuous gust front structure and new updraft/mesocyclone development occurs farther downshear (Fig. 3d). By 9300 s, the old updraft has completely dissipated (Fig. 3e) and the supercell has become virtually indistinguishable from its previous form around 5200 s.

Further evolution is nearly identical to that described previously. As a result of the reintensification of the RFD and near-ground mesocyclone between 9900 and 11 400 s, the gust front once again bows outward and a pronounced hook forms in the rainwater field (Fig. 3a). Downshear updraft development proceeds simultaneously (Fig. 3b), with the second complete occlusion (Fig. 3c) occurring at 11 700 s. The old updraft and mesocyclone again completely separate from the gust front (Fig. 3d), and the new updraft/mesocyclone develops to its east while the old updraft quickly decays (Fig. 3e). A third occlusion occurs near 13 500 s and subsequent storm evolution becomes more complex.

This study will focus on the storm structure and evolution associated with the first occlusion at 7200 s, although the second occlusion could be used because it proceeds similarly. In the next section, the analysis that led to the five-part conceptual model is presented.

4. Simulation results and analysis

a. Introduction

In this section, a detailed analysis of the occlusion process and associated mesocyclogenesis is presented. It has been proposed (e.g., Burgess et al. 1982) that secondary mesocyclogenesis in a cyclic supercell proceeds more rapidly after the initial occlusion as a result of development in the vicinity of a ''vorticity-rich environment.'' However, the presence of a residual cold pool and associated surface buoyancy gradients rather than the presence of near-ground vorticity from previous mesocyclones is found to be a crucial element of cyclic mesocyclogenesis. Since initial near-ground mesocyclogenesis appears to act by the same mechanism as subsequent mesocyclogenesis, we devote a significant amount of section 4b to its description.

b. Stage 1: Initial near-ground (<500 m) mesocyclogenesis in an incipient supercell

Figures 4a–d depict windowed horizontal and vertical cross sections through the simulated storm at 5100 s,

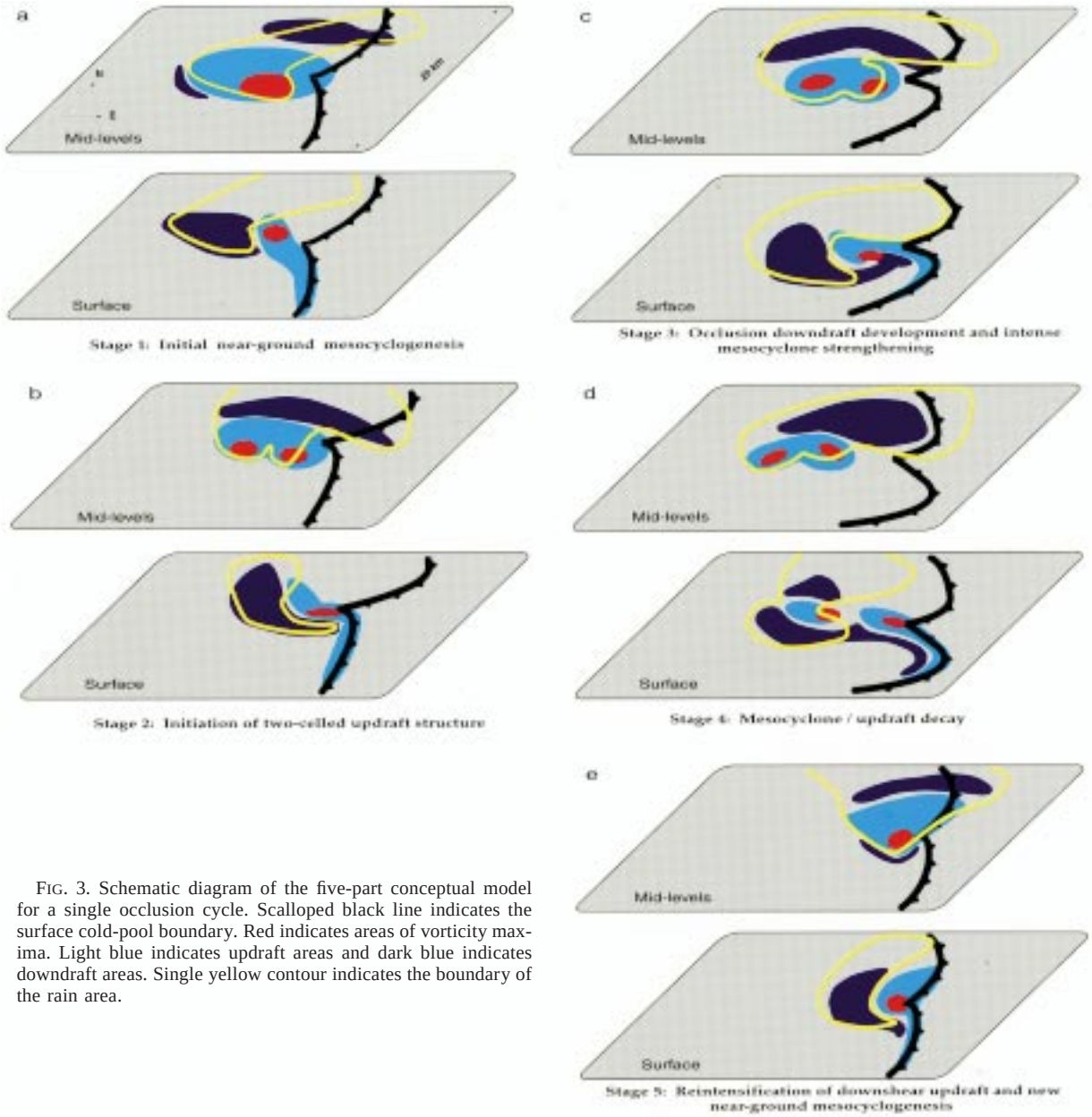

FIG. 3. Schematic diagram of the five-part conceptual model for a single occlusion cycle. Scalloped black line indicates the surface cold-pool boundary. Red indicates areas of vorticity maxima. Light blue indicates updraft areas and dark blue indicates downdraft areas. Single yellow contour indicates the boundary of the rain area.

prior to the first occlusion. At this time, the storm consists of a well-developed supercell with updrafts greater than 30 m s^{-1} and a mesocyclone (vertical vorticity >0.01 s^{-1}) that extends through the lowest 10 km of the storm. The RFD is prominent at the surface and at $z = 1.1$ km (Figs. 4a,b), but declines in strength with height and is only slightly evident at $z = 4$ km (Fig. 4c). This observation agrees with the conclusions of Knupp (1987), who found little evidence that downdrafts that reach the surface begin at heights greater than 4 km, as originally suggested by Lemon and Doswell (1979).

In order to aid the analysis, several time–height cross sections were constructed from the model data at 60-s intervals. These maxima–minima analyses are performed not over the entire domain, but over a manually selected subsection that includes only the storm of interest, and depict features that have been checked for vertical continuity. A time–height cross section of maximum downdraft (Fig. 5) shows that local extrema begin building upward and downward from approximately 1 km just prior to 5100 s. This observation is consistent with an RFD driven by the evaporation of falling precipitation. As a result of environmental storm-relative winds that veer with height and the presence of a mesocyclone, the negatively buoyant downdraft air falls

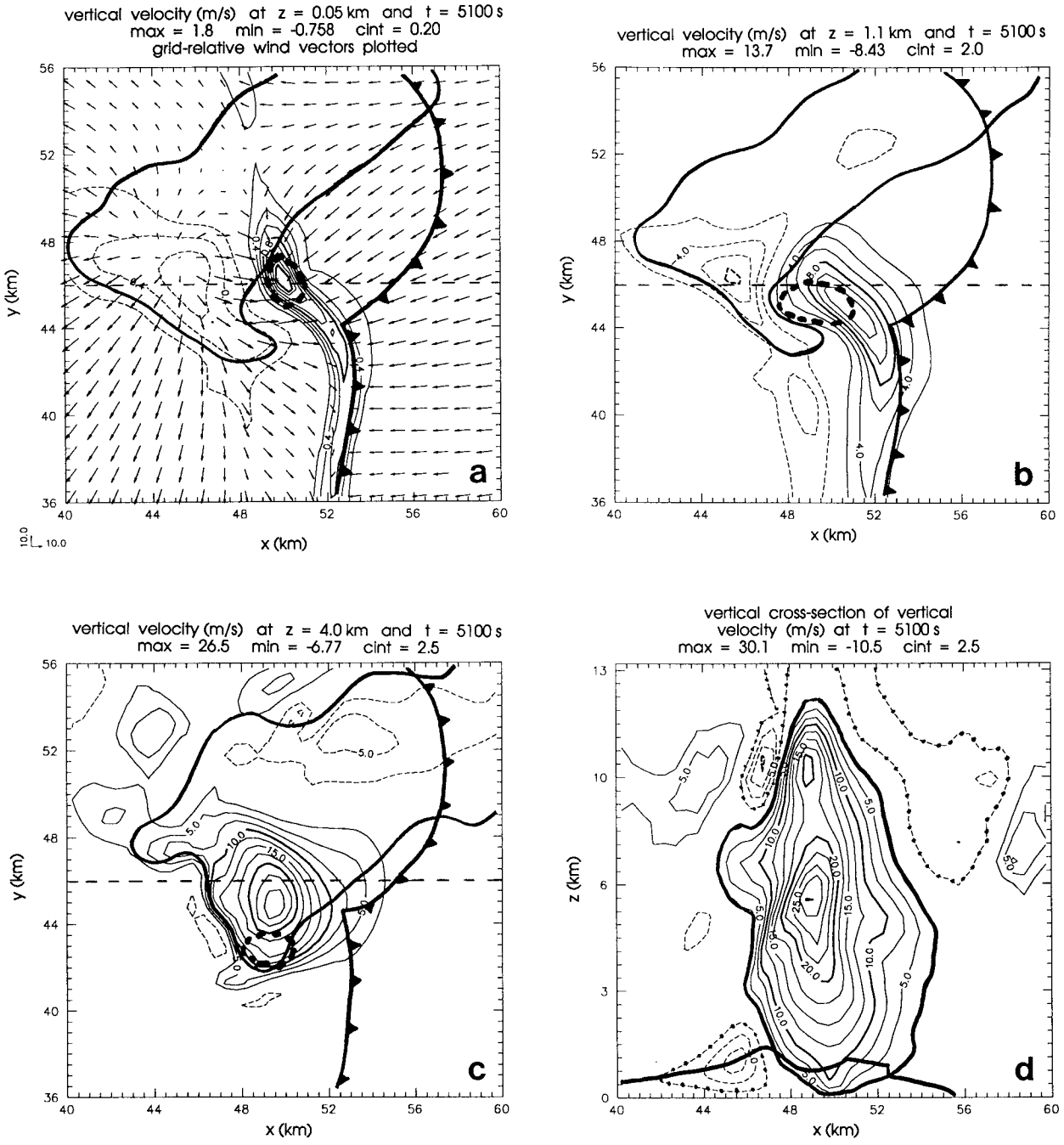

FIG. 4. (a) Horizontal cross section of vertical velocity at lowest grid point ($z = 50$ m) at $t = 5100$ s. Contour interval is 0.2 m s^{-1}. Surface cold-pool location (-1 K potential temperature perturbation contour) indicated by standard cold-front notation. Isoline of 1 g kg^{-1} rainwater-mixing ratio indicated by the single dark contour. Isoline of 0.01 s^{-1} vorticity value indicated by single dark dashed contour. Grid-relative wind vectors indicated. (b) Same as (a) except cross section taken at $z = 1.1$ km. Contour value of vertical velocity is 2.0 m s^{-1}. Rainwater isoline value is 1.0 g kg^{-1}. Vorticity isoline value is 0.01 s^{-1}. (c) Same as (a) except cross section taken at $z = 4$ km. Contour value of vertical velocity is 2.5 m s^{-1}. Rainwater isoline value is 1.0 g kg^{-1}. Vorticity isoline value is 0.015 s^{-1}. (d) Vertical cross section of vertical velocity taken through straight dashed line in (a)–(c). Contour value of vertical velocity is 2.5 m s^{-1}. Single dark surface contour indicates -1 K perturbation potential temperature (surface cold pool).

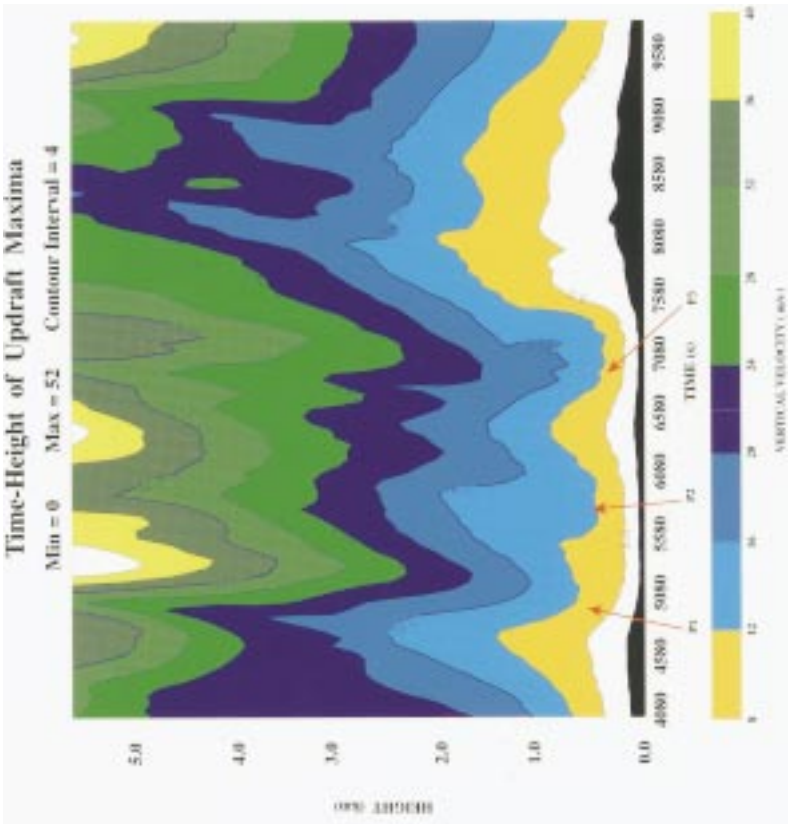

FIG. 5. Time–height cross section of vertical-velocity minima (m s^{-1}). Contour interval is 3 m s^{-1}. Minima were calculated from unsmoothed 1-min data only in the relevant area of the domain.

FIG. 6. Time–height cross section of vertical-velocity (m s^{-1}). Contour interval is 3 m s^{-1}. Maxima were calculated from unsmoothed 1-min data only in the relevant area of the domain. Updraft pulses 1–3 are indicated as P1, P2, and P3, respectively.

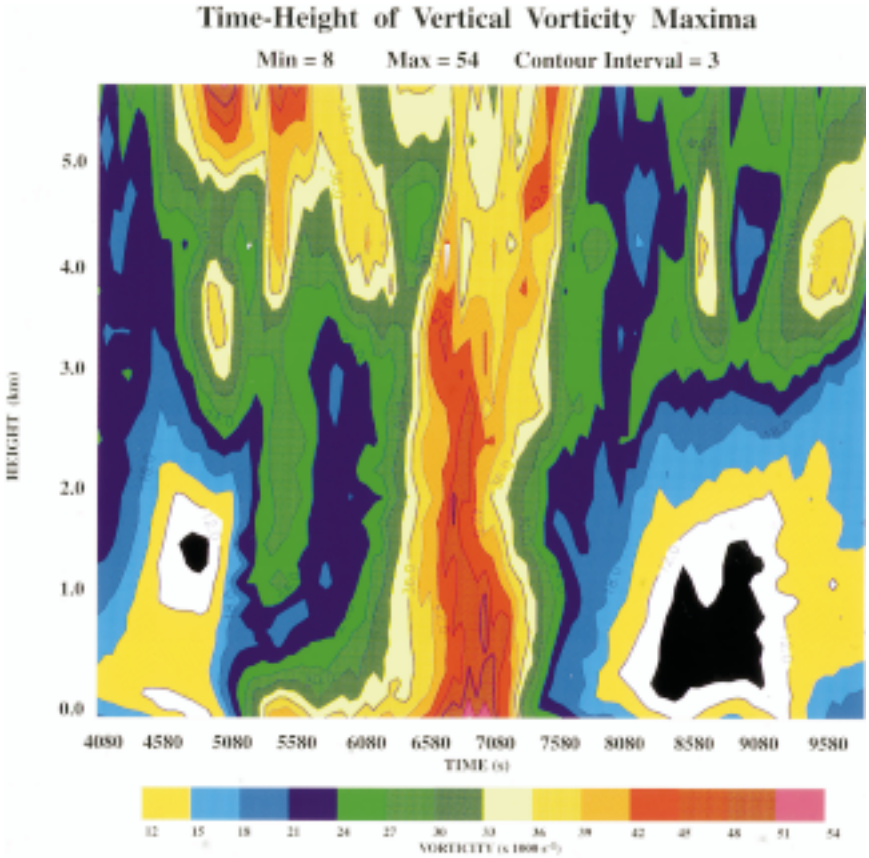

FIG. 7. Time–height cross section of vertical-vorticity maxima ($\times 10^3$). Contour interval is 3 $\times$ 10^{-3} s^{-1}. Maxima were calculated from unsmoothed 1-min data only in the relevant area of the domain.

cyclonically around the main updraft, resulting in a characteristic hook shape in the rainwater field (Davies-Jones and Brooks 1993) (Figs. 4a,b). Nearly coincident with the upward-building RFD is the initiation of the first (P1) of three updraft pulses (Fig. 6). Although it is difficult to discriminate cause and effect, the initiation of this first pulse is consistent with enhanced convergence along the gust front as a result of RFD propagation toward the east.

A time–height cross section of maximum vertical vorticity (Fig. 7) shows that, although vorticity remains above mesocyclone criteria (0.01 s^{-1}) above 2 km, the mesocyclone below this height strengthens from approximately 0.01 to 0.02 s^{-1} between 4800 and 5100 s. In order to clarify the origins of the vorticity, backward trajectories are calculated from the 1-min model data using a three-step predictor-corrector method with a time step of 1 s. Parcel quantities such as vorticity are calculated from linear spatial and temporal interpolation of the original three-dimensional fields. The validity of the vorticity equation decomposition is verified by comparing the evolution of the Lagrangian derivative, as calculated from the sum of the individual forcing terms, to that calculated from the interpolated field. Parcels in which these two quantities differ significantly are rejected from the analysis. In all cases, the trajectory calculations are performed with grid-relative winds. Since grid-relative storm motion is very slow and the integration time is short, these trajectory calculations are approximately storm relative.

A 3 $\times$ 3.5 km rectangular group of parcels centered on the near-ground mesocyclone at z = 150 m is integrated back 900 s from 5100 to 4200 s. Figure 8a shows the presence of two source regions for parcels entering the near-ground mesocyclone, a result consistent with previous numerical studies (Klemp and Rotunno 1983; Rotunno and Klemp 1985; Davies-Jones and Brooks 1993; Wicker and Wilhelmson 1995). The first region is centered northwest of the mesocyclone and consists of parcels that descend cyclonically through the outer edges of the RFD and then rise back into the near-ground mesocyclone. The second source region is located east and northeast of the gust front and consists of parcels that travel into the mesocyclone along paths that are nearly horizontal (vertical displacements are usually less than 100 m). A plot of horizontal vorticity vectors (Fig. 8b) suggests that all parcels originating from the western region may have a significant com-

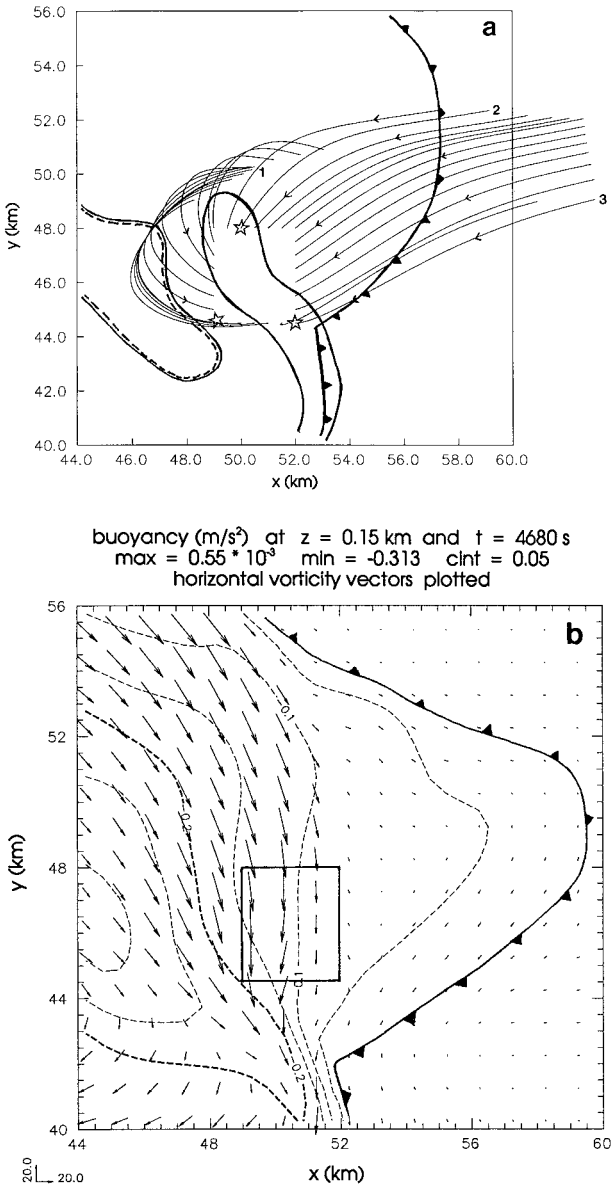

FIG. 8. (a) Projection of the three-dimensional backward trajectories toward the near-ground mesocyclone. Parcels were started from $z = 150$ m and integrated from $t = 5100$ to 4200 s. Parcels were initially spaced 500 m apart. Scalloped line indicates cold-pool boundary. Solid line depicts updraft area. Dashed line depicts downdraft area. Initial locations of the parcels discussed in the text are numbered in the order they are presented. Final locations are labeled with a star. (b) Horizontal cross section of buoyancy contours and horizontal vorticity vectors at $z = 150$ m for $t = 4680$ s. Buoyancy contour interval is 0.05 m s^{-2}. Rectangular ring of parcel starting points is indicated.

ponent of streamwise vorticity before entering the near-ground updraft and mesocyclone. In addition, some of the parcels entering the northern edge of the mesocyclone from the eastern source region may also have a significant streamwise component.

In order to better understand the vorticity dynamics associated with each parcel, we consider the Lagrangian equations for the horizontal and vertical components of vorticity. Since we focus only on near-ground mesocyclogenesis, the Boussinesq approximation is applied. It is convenient to formulate our equations in seminatural coordinates, where (**s**, **n**, **k**) represent orthonormal basis vectors (Lilly 1982), with the vector wind $\mathbf{V} = (V_H, 0, w)$. If turbulent mixing and diffusion are neglected, the equation for vertical vorticity (ζ) is given by

$$\frac{d\zeta}{dt} = \boldsymbol{\omega}_h \cdot \boldsymbol{\nabla} w + \zeta \frac{\partial w}{\partial z}, \tag{1}$$

where $\boldsymbol{\omega}$ is the three-dimensional vorticity vector and the terms on the right-hand side represent tilting of horizontal vorticity into the vertical and vertical stretching of vertical vorticity, respectively. It is important to realize that the customary tilting and stretching descriptors are somewhat misleading, as both terms stretch and tilt vortex tubes (Davies-Jones 1982).

With similar approximations, the equations for the horizontal streamwise (ω_s) and crosswise (ω_n) vorticity are

$$\frac{d\omega_s}{dt} = \omega_n \frac{d\psi}{dt} + \boldsymbol{\omega} \cdot \boldsymbol{\nabla} V_H + \frac{\partial B}{\partial n} \tag{2}$$

$$\frac{d\omega_n}{dt} = -\omega_s \frac{d\psi}{dt} + \boldsymbol{\omega} \cdot (V_H \boldsymbol{\nabla} \psi) - \frac{\partial B}{\partial s}, \tag{3}$$

where the horizontal direction of a parcel is defined as $\psi = \tan^{-1}(v/u)$, and B represents buoyancy. The first term on the right-hand side of both equations represents the exchange between streamwise and crosswise vorticity (without changes in the magnitude of vorticity) as parcels change direction in the horizontal plane (Scorer 1978). The second and third term of each equation represent the rate of change of streamwise/crosswise vorticity from the stretching and tilting of vortex tubes, and baroclinic vorticity generation, respectively.

Consider a parcel at the southwest corner of the rectangle in Fig. 8a ($x = 49.0$ km, $y = 44.5$ km, $z = 0.15$ km) that originates in the source region to the northwest of the mesocyclone. We suggest that this example is representative of the vorticity dynamics that characterize the parcels on the western and southwestern portions of the mesocyclone. Figure 9a, which shows the altitude of the parcel as a function of time, indicates that the parcel first descends in a nearly linear fashion from a relatively shallow height (<500 m) with a small but negative component of vertical vorticity (Fig. 9b). The vorticity decreases slightly through the first 100 m (4200–4564 s) of descent as the environmental vortex lines are tilted downward. Throughout the rest of the descent, vertical vorticity increases and actually changes sign before the parcel reaches its nadir and enters the edge of the near-ground mesocyclone.

To understand the importance of this result, Fig. 10 shows four types of vorticity calculated along the descending parcel's trajectory: the vertical vorticity (ζ),

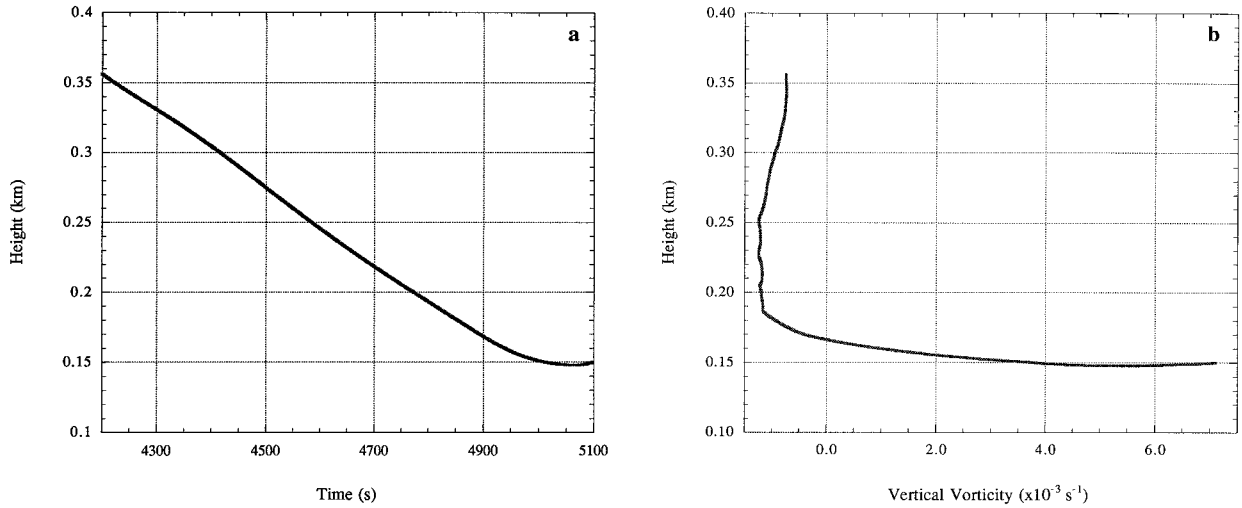

FIG. 9. (a) Time (s) vs height (km) plot of a parcel originating at the lower-left corner ($x = 49.0$ km, $y = 44.5$ km, $z = 0.15$ km) of the initial trajectory rectangle indicated in Fig. 8a. (b) Vorticity ($\times 10^{-3}$ s^{-1}) vs height (km) plot of the same parcel as in (a).

the streamwise vorticity (ω_s), the crosswise vorticity (ω_n), and the magnitude of the total three-dimensional vorticity ($|\boldsymbol{\omega}|$). At the beginning of the parcel's descent, the vertical vorticity is nearly zero, but the total vorticity has a magnitude of approximately 0.013 s^{-1}. As the parcel starts to descend, the streamwise vorticity is small and slightly negative, with most of the parcel's total vorticity contained in the crosswise component. As the parcel continues its downward motion, the vertical vorticity remains small (but increases), while the streamwise and crosswise vorticity both gradually increase. Below 200 m ($t > 4772$ s), the crosswise vorticity begins to decrease, while the streamwise vorticity rapidly grows, eventually peaking just above $z = 150$ m ($t = 5000$ s). With further descent, the horizontal vorticity is amplified, and the vortex line becomes more and more parallel to the direction of parcel motion. Just above $z = 150$ m, nearly all of the vorticity is parallel to the trajectory. Referring back to Fig. 9, we note that at this level, the vertical vorticity is slightly positive and increasing, but the trajectory is still slightly downward. Therefore, vortex lines are being turned upward during descent. This is similar to the mesocyclogenesis mechanism proposed by Davies-Jones and Brooks (1993) and Davies-Jones (1996).

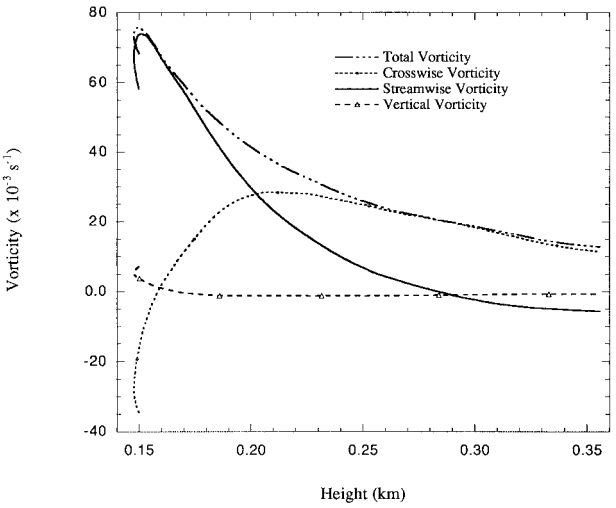

FIG. 10. Plots of the vertical vorticity ζ, streamwise vorticity ω_s, crosswise vorticity ω_n, and total three-dimensional vorticity $|\boldsymbol{\omega}|$, with height (km) for the parcel described in Fig. 9. Vorticity values are $\times 10^{-3}$ s^{-1}.

Below 150 m ($t > 5000$ s), the vertical vorticity begins to increase rapidly, while the total vorticity, streamwise vorticity, and crosswise vorticity quickly decrease as the parcel approaches its lowest level and then begins to turn upward into the mesocyclone. Although the parcel's total vorticity $|\boldsymbol{\omega}|$ is decreasing, vortex lines are being rapidly tilted/stretched into the vertical at a large inclination angle to the mostly horizontal trajectories.

To fully understand what particular motions are contributing to the change in the parcel's vertical vorticity, it is necessary to consider the terms from the vorticity-tendency equations. Figure 11 displays the tilting and stretching/convergence terms in the vertical-vorticity equation from (1) as a function of height. Throughout most of the parcel's descent above 200 m (4200–4772 s), the tilting term is negative and the stretching term is positive but smaller in magnitude, resulting in a slight decrease in vertical vorticity. Below 200 m, rapid changes occur within a 300-s time period. The stretching term decreases, becoming slightly negative as the parcel slows down and reaches the lowest part of its trajectory. As the parcel accelerates back upward into the mesocyclone, this term rapidly increases. The tilting term also increases rapidly, peaking as the parcel motion changes from downward to upward. The vertical stretch-

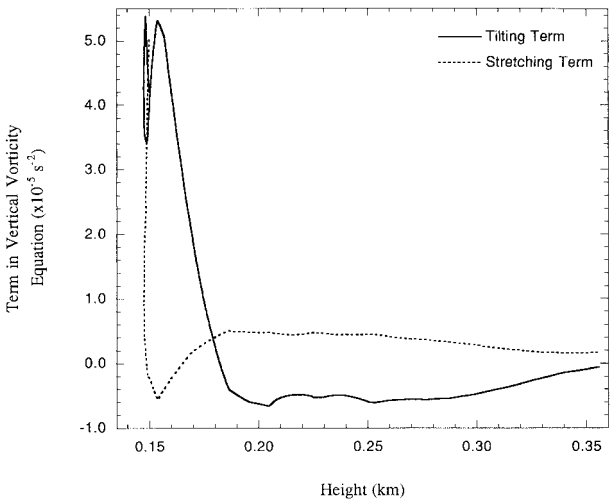

FIG. 11. Plots vs height (km) of the vertical tilting term and vertical convergence/stretching term in the vertical vorticity equation. Curves are for the parcel described in Fig. 9. Vorticity terms are $\times 10^{-5}$ s^{-2}.

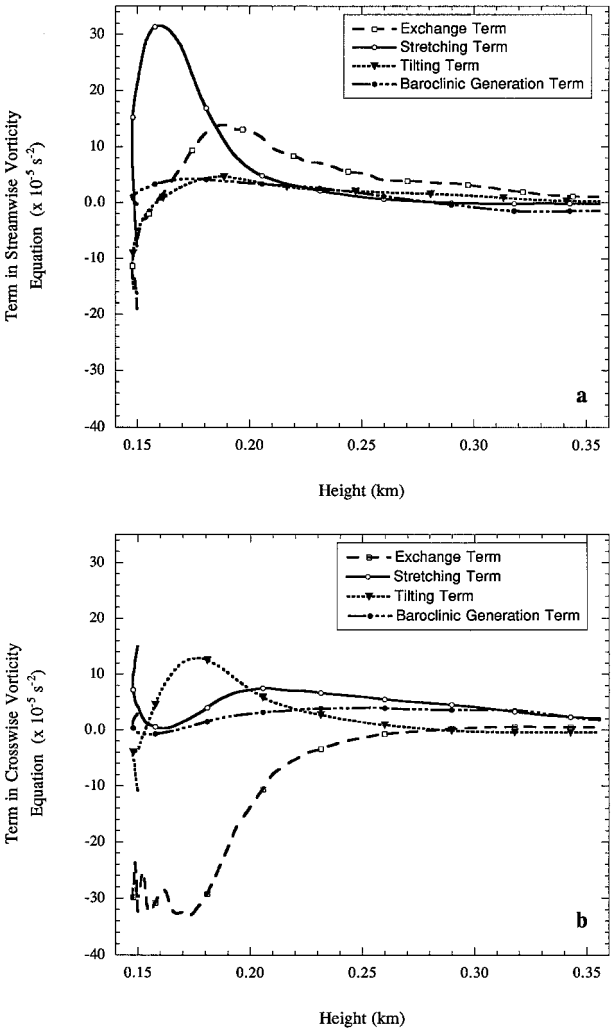

FIG. 12. (a) Plots vs height (km) of the streamwise exchange term, stretching term, tilting term, and baroclinic generation term in the streamwise vorticity equation. Curves are for the parcel described in Fig. 9. Vorticity terms are $\times 10^{-5}$ s^{-2}. (b) Plots vs height (km) of the crosswise exchange term, stretching term, tilting term, and baroclinic generation term in the crosswise vorticity equation. Curves are for the parcel described in Fig. 9. Vorticity terms are $\times 10^{-5}$ s^{-2}.

ing/convergence term becomes large once the trajectory turns upward.

In order to determine the origins of the horizontal vorticity, which is tilted into and stretched in the vertical, Figs. 12a,b display the terms from the streamwise (2) and crosswise (3) vorticity equations along the same trajectory. As noted previously (Fig. 10), above 250 m (4200–4584 s) the streamwise vorticity increases steadily throughout descent, while the crosswise vorticity increases less rapidly. From Fig. 12a, streamwise stretching is initially near zero, streamwise baroclinic generation is slightly negative, and streamwise tilting is slightly positive. The exchange term, which converts crosswise vorticity to streamwise vorticity, dominates. In the crosswise direction, stretching and baroclinic generation are initially dominant. Therefore, as the parcel begins its descent, most of the horizontal vorticity is generated baroclinically and by stretching in the crosswise direction. This vorticity is then reoriented into the streamwise direction as the parcel curves cyclonically.

Between 250 and 200 m (4584–4772 s), important changes occur (Figs. 12a,b). In the streamwise direction, baroclinic generation becomes positive, and the exchange and stretching terms both increase. Nonetheless, the exchange term is still dominant. In the crosswise direction, baroclinic generation remains positive (but weakens slightly), tilting and stretching increase, and exchange decreases. Therefore, the cyclonic motion of the parcel is important for two reasons: first, it allows the exchange of crosswise-to-streamwise vorticity to continue; and second, it results in the parcel becoming more parallel to the buoyancy contours, thereby allowing baroclinic generation to occur in the streamwise direction. In addition, we note that the effect of horizontal acceleration into the mesocyclone (as manifested in the streamwise stretching) starts to become a dominant factor.

Below 200 m ($t > 4772$ s), very rapid changes occur in all terms. The crosswise vorticity decreases rapidly and the streamwise vorticity approximately triples (Fig. 10). From Fig. 12, we see that the large increase in the parcel's streamwise vorticity results mainly from stretching, which dominates during the final 300 s of the trajectory. Although tilting and stretching become negative below 160 m ($t > 4938$ s), the baroclinic generation remains positive. The large decrease in crosswise vorticity results mainly from the exchange term. These observations suggest that most of the streamwise vorticity that is tilted and stretched into the vertical arises from two sources: the horizontal acceleration experi-

enced by the parcel as it approaches the near-ground mesocyclone and the curvature of the motion of the parcel (which determines the exchange term).

Parcels originating in the eastern source region have a more varied evolution and are more prone to errors in the trajectory computation as a result of very strong gradients in the vorticity-tendency terms. In general, these parcels show smaller changes in all three components of vorticity as they travel nearly horizontally toward the mesocyclone.

Considering other parcels from the eastern source region analyzed but not discussed in detail here, we can separate their behavior into two categories: parcels that exhibit strong streamwise baroclinic generation through the latter portion of their trajectory and those that do not. The former consist of parcels that end their trajectories along the northern border of the mesocyclone in Fig. 8a, approximately parallel to the buoyancy contours (Fig. 8b).

The evolution of one such representative parcel (x = 50.0 km, y = 48.0 km, z = 0.15 km) is displayed in Fig. 13. Streamwise vorticity is the dominant component for these parcels throughout their evolution (Fig. 13c). As they approach the mesocyclone, vertical vorticity increases by approximately equal amounts of stretching and tilting, with stretching dominating as the parcels begin to accelerate upward. An examination of the horizontal-vorticity terms shows that streamwise baroclinic generation is the primary source of the horizontal vorticity, which is subsequently tilted and stretched during mesocyclogenesis.

The second category of parcel trajectories end on the eastern edge of the mesocyclone (Fig. 8a), where the vorticity is mostly crosswise (Fig. 8b). The evolution of one such representative parcel (x = 52.0 km, y = 44.5 km, z = 0.15 km) is displayed in Fig. 14. These parcels travel most of their path with near-zero values of vertical vorticity, and with small values of streamwise/crosswise vorticity. As they approach the mesocyclone, the small components of horizontal vorticity are tilted and then stretched into the vertical, with stretching again dominating as the parcels near the mesocyclone. In contrast to the other parcels, no single forcing term dominates, and most of the horizontal vorticity is generated by small amounts of crosswise and streamwise baroclinic generation and stretching, followed by conversion via the exchange term.

Time–height plots of the in-storm maximum tilting and stretching terms are shown in Figs. 15 and 16. Prior to 5100 s, tilting and stretching are minimal in the lowest kilometer. After 5100 s, the RFD strengthens and initiates stronger convergence along the gust front, subsequently resulting in the first updraft pulse (P1 in Fig. 6). Figure 15 shows that this pulse coincides with the appearance of tilting maxima greater than 9×10^{-5} s^{-2} just above the surface. More significantly, it also coincides with strong maxima in convergence/stretching, with values exceeding 100×10^{-5} s^{-2} near the ground

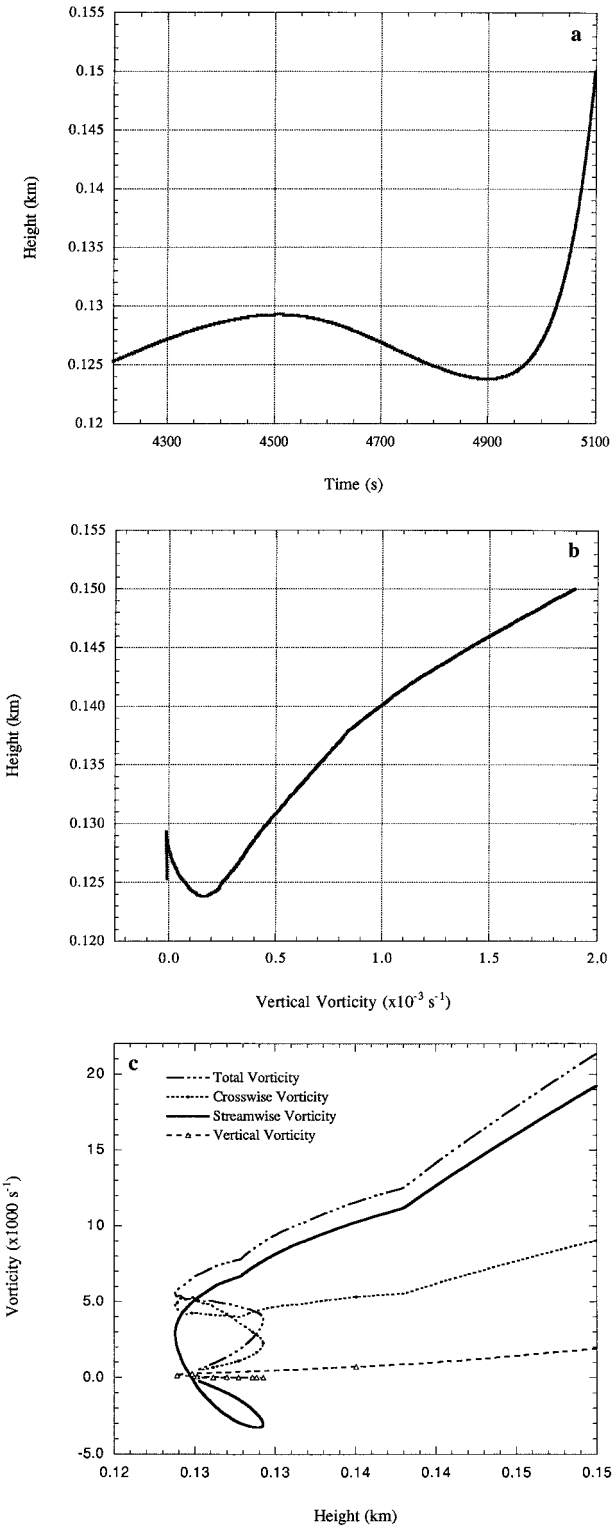

FIG. 13. (a) Time (s) vs height (km) plot of a parcel originating on the northern boundary of the initial trajectory rectangle (x = 50.0 km, y = 48.0 km, z = 0.15 km) indicated in Fig. 8a. (b) Vorticity ($\times 10^{-3}$ s^{-1}) vs height (km) plot of the same parcel as in (a). (c) Plots of the vertical vorticity ζ, streamwise vorticity ω_s, crosswise vorticity ω_n, and total three-dimensional vorticity $|\boldsymbol{\omega}|$, with height (km) for the parcel described in (a). Vorticity values are $\times 10^{-3}$ s^{-1}.

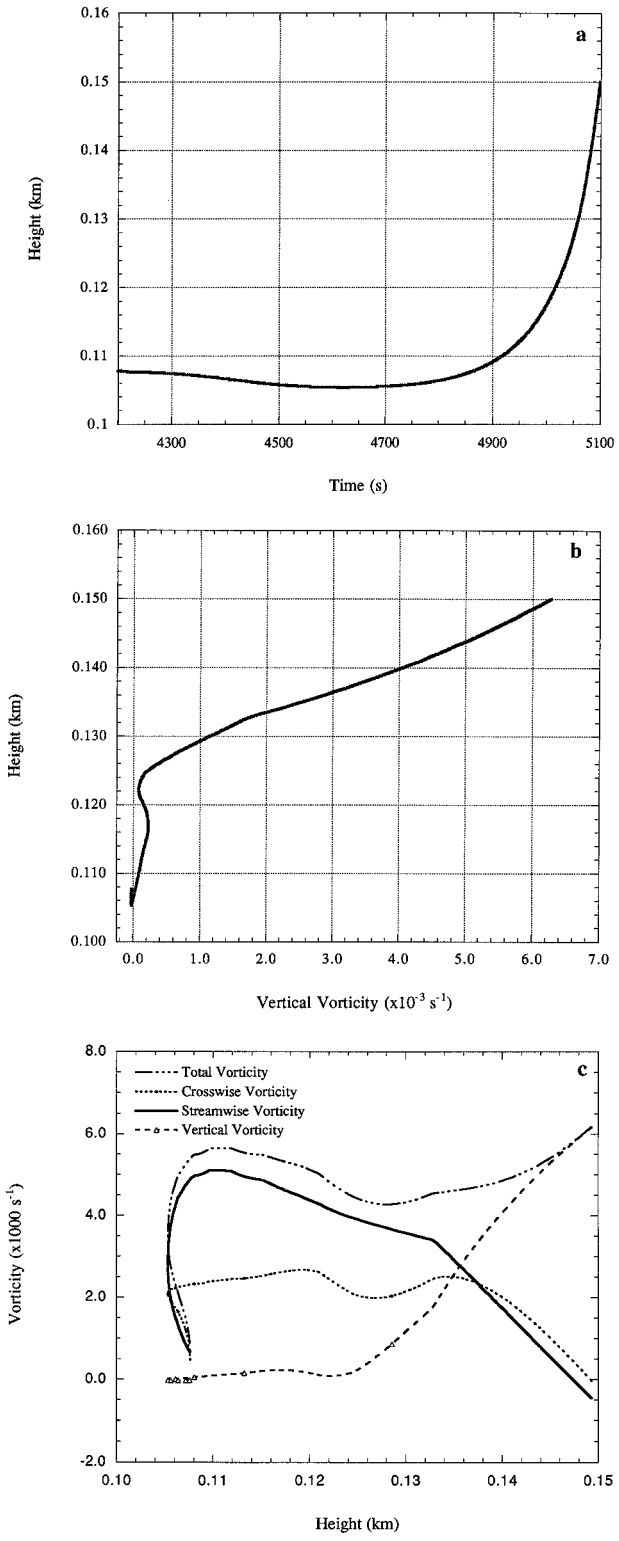

FIG. 14. (a) Time (s) vs height (km) plot of a parcel originating on the eastern boundary of the initial trajectory rectangle ($x = 52.0$ km, $y = 44.5$ km, $z = 0.15$ km) indicated in Fig. 8a. (b) Vorticity ($\times 10^{-3}$ s^{-1}) vs height (km) plot of the same parcel as in Fig. 14a. (c) Plots of the vertical vorticity ζ, streamwise vorticity ω_s, crosswise vorticity ω_n, and total three-dimensional vorticity $|\boldsymbol{\omega}|$, with height (km) for the parcel described in (a). Vorticity values are $\times 10^{-3}$ s^{-1}.

(Fig. 16). Since the convergence term rapidly overtakes the tilting term, the magnitude of the vertical acceleration near the ground is the determining factor in the rapidity of near-ground mesocyclogenesis once a parcel acquires vertical vorticity (as shown in Fig. 7).

From the analysis described above, we see that the evaporatively generated near-ground buoyancy gradient (Fig. 8b) appears necessary for initial near-ground mesocyclogenesis, a result demonstrated previously (Rotunno and Klemp 1985; Davies-Jones and Brooks 1993; Wicker and Wilhelmson 1995). As parcels travel near this boundary from source regions to the northwest of the updraft, they gain (from crosswise baroclinic generation and crosswise stretching) horizontal vorticity that can be reoriented into the streamwise direction, further intensified via horizontal stretching, and then tilted into the vertical. An important difference in this analysis is that for most parcels (except for some that enter the northern part of the mesocyclone from the eastern source region), streamwise baroclinic generation is not the dominant term in the horizontal-vorticity tendency but is a secondary effect that continually generates the horizontal vorticity that is strongly intensified by the near-ground horizontal convergence into the mesocyclone (streamwise stretching). The parcel analyses suggest that tilting into the vertical is initially dominant just as the parcels begin to ascend, but that stretching soon dominates as the parcels accelerate upward through the mesocyclone.

Positive vertical-vorticity generation in descending parcel trajectories (those from the western source region) is also shown to occur in this simulation. This is similar to results presented by Davies-Jones and Brooks (1993), but for a much later time in the supercell's evolution. However, in contrast with their findings, our analysis shows that parcels on the eastern side of the mesocyclone attain vertical vorticities comparable to those on the western side. Similar to Davies-Jones and Brooks (1993), one notes that the contribution to the circulation around the rectangle from winds on the east side is *negative* (Fig. 8a).

These findings are also similar to the results of Grasso and Cotton (1995), who conjectured that near-ground positive vertical vorticity was being generated along cyclonically curved parcel trajectories that traveled through the downdraft. However, this contrasts with the high-resolution simulations of Wicker and Wilhelmson (1995), who did not observe a similar mechanism for the generation of vorticity near the surface.

c. Stage 2: Initiation of the two-celled updraft structure

Figure 17 depicts windowed horizontal and vertical cross sections through the evolving supercell at 5820 s, prior to the first occlusion but after the mesocyclone below 1 km has strengthened to an intensity comparable to that at midlevels (Fig. 7). Near the surface (Fig. 17a),

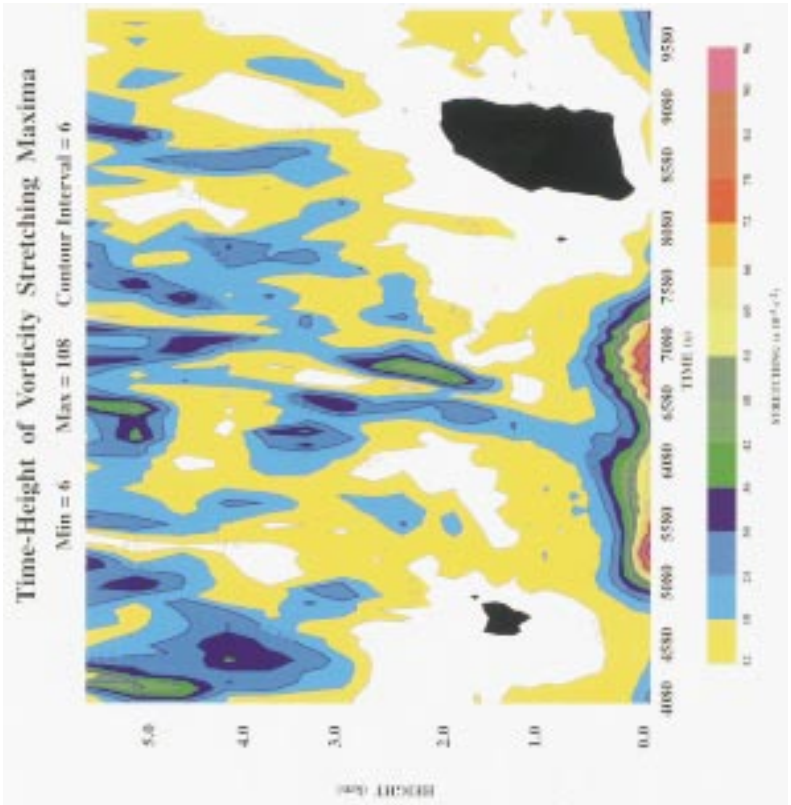

FIG. 16. Time–height cross section of the maxima in the convergence/stretching term of the vertical vorticity tendency equation ($\times 10^5$). Contour interval is 6×10^{-5} s^{-2}. Maxima were calculated from unsmoothed 1-min data only in the relevant area of the domain.

FIG. 15. Time–height cross section of the maxima in the tilting term of the vertical vorticity equation ($\times 10^5$). Contour interval is 3×10^{-5} s^{-2}. Maxima were calculated from unsmoothed 1-min data only in the relevant area of the domain.

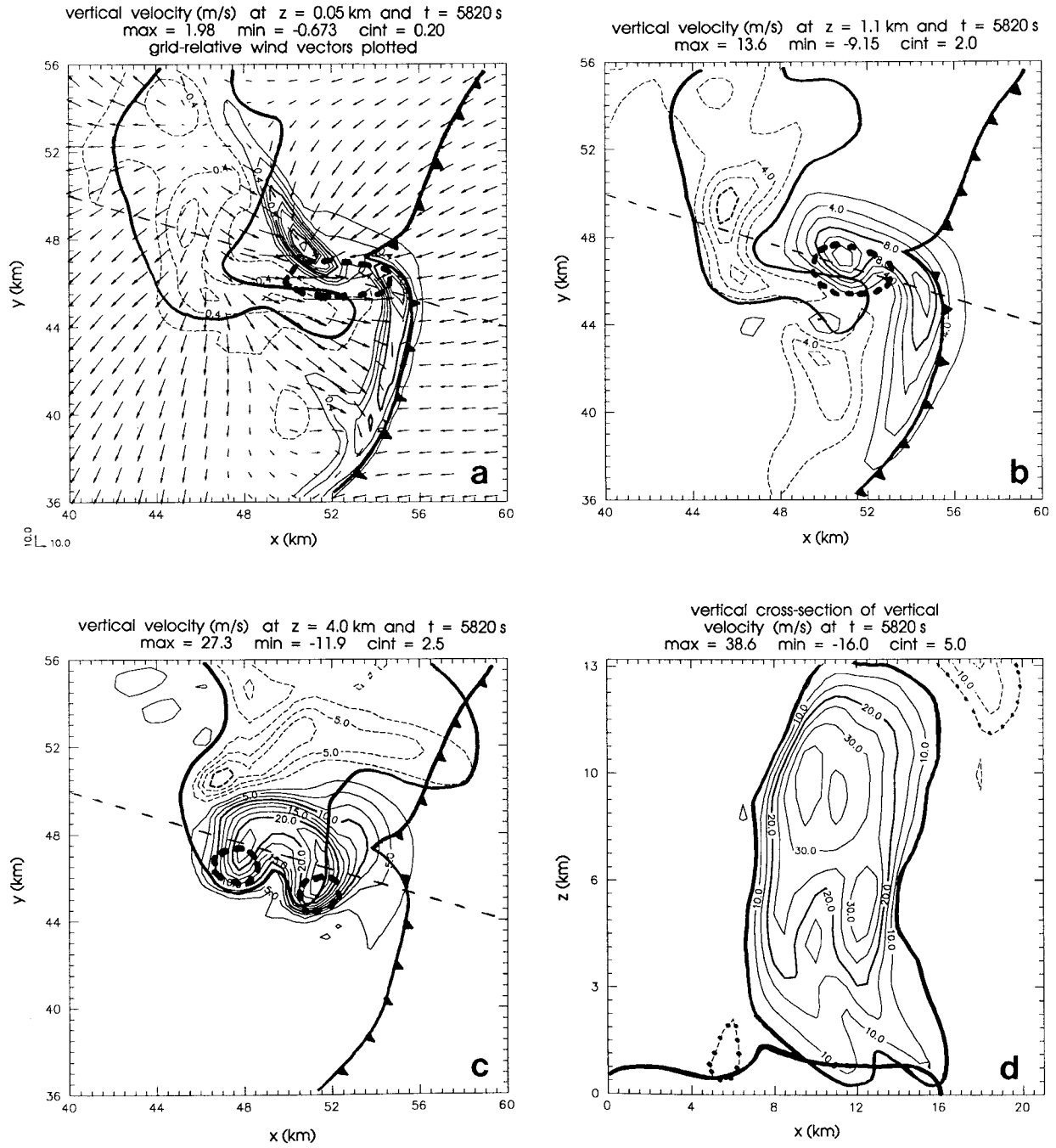

FIG. 17. Same as in Figs. 4a–d except for $t = 5820$ s. (d) Contour interval has increased to 5 m s^{-1}.

the RFD has pushed the gust front outward several kilometers from its previous position (cf. Fig. 4a). This effect, combined with the near-ground circulation around the mesocyclone, rotates the original updraft into a more east–west orientation. Convergence along the gust front is weaker but no longer as localized as at $t = 5100$ s. This convergence over a larger area is associated with the formation of a second updraft pulse (P2) in the original updraft ($x = 51$ km, $y = 48$ km in Fig. 6). The gust front motion also has the effect of initiating a secondary updraft maximum near the inflection point at $x = 55$ km, $y = 46$ km, southeast of the original updraft. This secondary updraft is apparent up to 4 km (Fig. 17c), above which it merges into a single larger updraft (Fig. 17d). It is apparent from Fig. 17 that the two-celled updraft structure is not a result

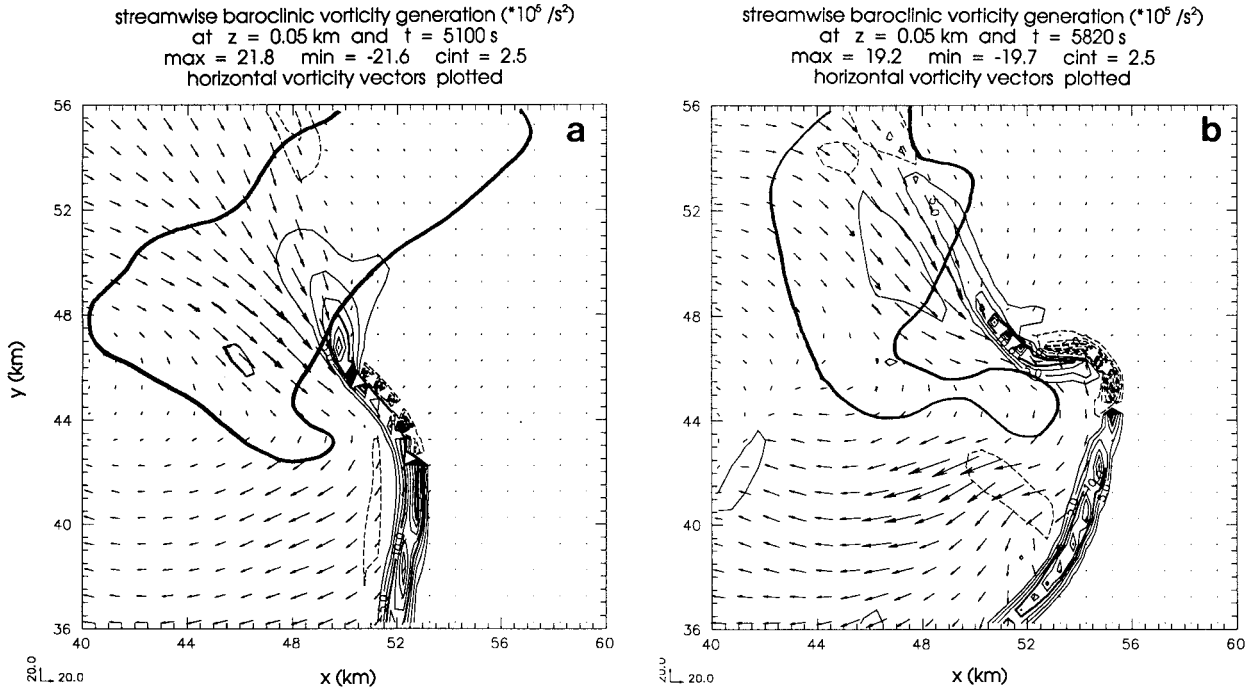

FIG. 18. (a) Horizontal cross section of the streamwise baroclinic horizontal vorticity generation term ($\times 10^5$) at the lowest grid point ($z = 50$ m) at $t = 5100$ s. Contour interval is 2.5×10^{-5}. Horizontal vorticity vectors are shown. Isoline of 1 g kg^{-1} rainwater mixing ratio indicated by the single dark contour. (b) Same as in (a) except at $t = 5820$ s.

of splitting but is an eastward redevelopment arising from the formation of a new updraft at low levels along the gust front.

Figure 7 shows that vertical vorticity at the lowest levels has decreased slightly between 5600 and 6100 s but has developed upward in the lowest kilometer. Maxima at each level in the convergence term in the vertical-vorticity equation (Fig. 16) also show a decrease in magnitude near the ground, but increases aloft in conjunction with the second updraft pulse (Fig. 6). The tilting (Fig. 16) and vertical advection of vertical vorticity (not shown) also show small increases associated with the second updraft pulse, but their magnitudes are much smaller than the convergence/stretching term (12×10^{-5} s^{-2} vs 60×10^{-5} s^{-2}). A plot of the streamwise baroclinic generation field at 5100 and 5820 s (Fig. 18) shows that local maxima are concentrated along the near-ground buoyancy (θ_e) gradient, with the highest horizontal vorticities displaced slightly to the northwest. Therefore, baroclinic generation continues to produce horizontal vorticity that can be tilted and stretched throughout this time period.

d. Stage 3: Development of the occlusion downdraft and subsequent intense mesocyclone strengthening

Throughout the period $t = 5600$ to 6600 s, the largest values of vorticity occur near the surface (Fig 7). As demonstrated by Klemp and Rotunno (1983), the associated gradient in vertical vorticity can dynamically induce a downward-directed vertical pressure-gradient force (VPGF). Figure 19 shows that such a force, physically small in extent and located at $x = 54$ km, $y = 47.5$ km, approximately triples in magnitude between $t = 6300$ and 6600 s. Coincident with this increase is the development of an occlusion downdraft, centered just north of the maximum in downward VPGF (Fig. 19b; $x = 55$ km, $y = 49$ km), which deforms the occluding gust front into a circular arc. This feature also merges with the RFD (Fig. 19b), an observation previously noted by Wicker and Wilhelmson (1995). The occlusion downdraft does not contribute to the time–height diagram of downdraft maxima (Fig. 5) since its magnitude is smaller than that of the RFD.

The horizontal cross sections at 6600 s in Figs. 20a,b show that the occlusion downdraft extends upward through 1 km but is not present at 4 km. By this time, the mesocyclone has taken on a divided structure, with the updraft on its west side and the occlusion downdraft on its eastern side. This behavior is also consistent with previous observations and simulations (e.g., Lemon and Doswell 1979; Wicker and Wilhelmson 1995). The two-celled updraft structure is still visible at $z = 4$ km (Figs. 20c,d), with the secondary downshear development resulting from convergence along the eastern part of the gust front. The shallow (<4 km) RFD is also still visible in the cross section (Fig. 20d).

The occlusion downdraft has several important effects. First, its interaction with the lower portion of the

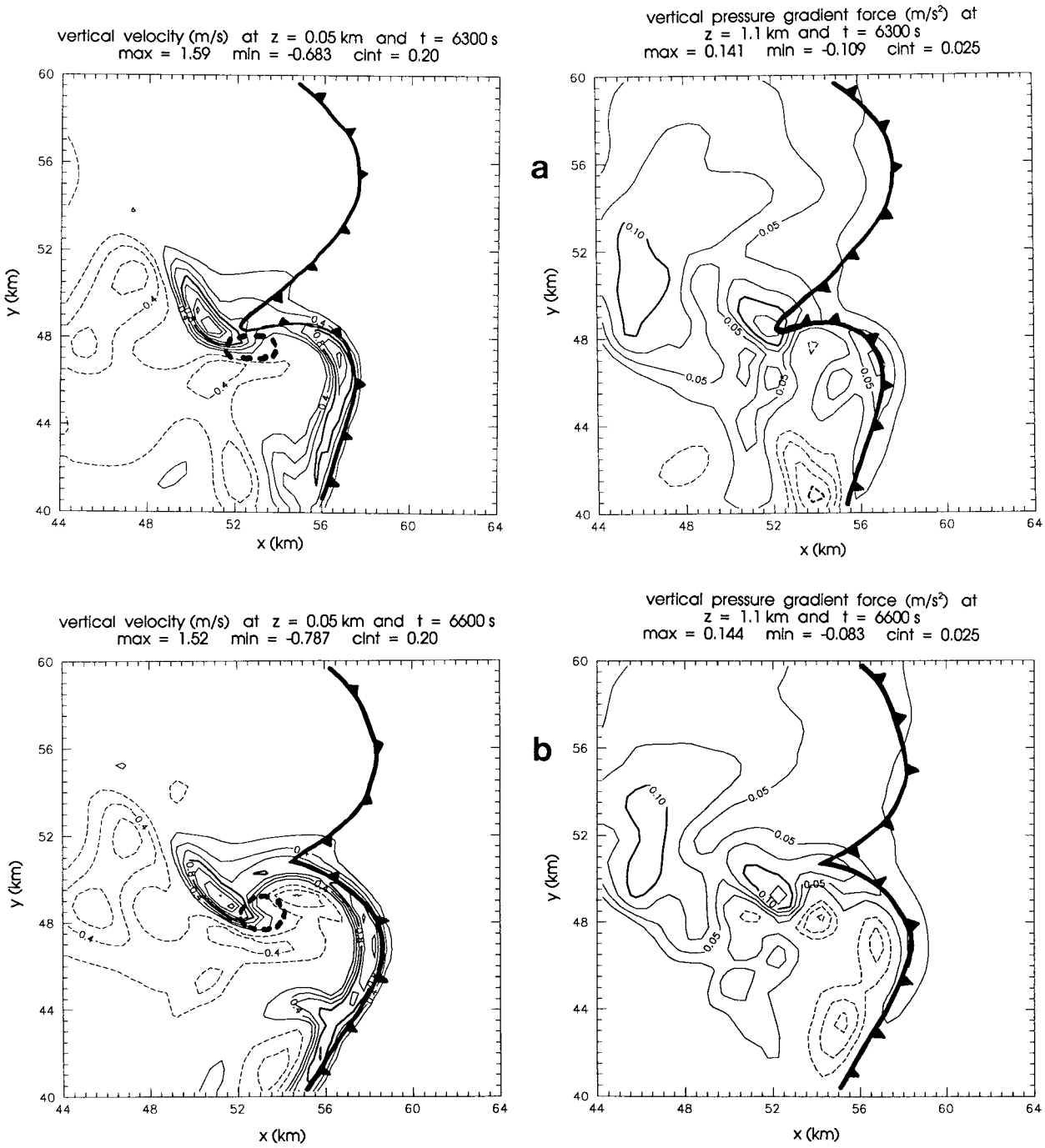

FIG. 19. (a) Horizontal cross section of vertical velocity at the lowest grid point and the VPGF at 1.1 km for $t = 6300$ s. Contour interval of vertical velocity is 0.2 m s^{-1}. Contour interval of VPGF is 0.025 m s^{-2}. (b) Same as in Fig. (a) except for $t = 6600$ s.

occluding updraft initiates the third and final updraft pulse (P3 in Fig. 6), which occurs immediately after the occlusion downdraft reaches the ground at 6600 s. This new pulse leads to mesocyclone intensification (Fig. 7) throughout a significant depth (0–5 km) and gives the appearance that the midlevel mesocyclone above 5 km has suddenly ''connected up'' with the mesocyclone at lower levels. Vorticity below 1 km rapidly increases from 38×10^{-3} s^{-1} to 54×10^{-3} s^{-1} after 6600 s and remains significantly larger than midlevel vorticity. The convergence term appears to be the dominant cause for this increase below 1 km.

Figure 16 shows that a new upward-building maximum in the convergence term coincides with the arrival

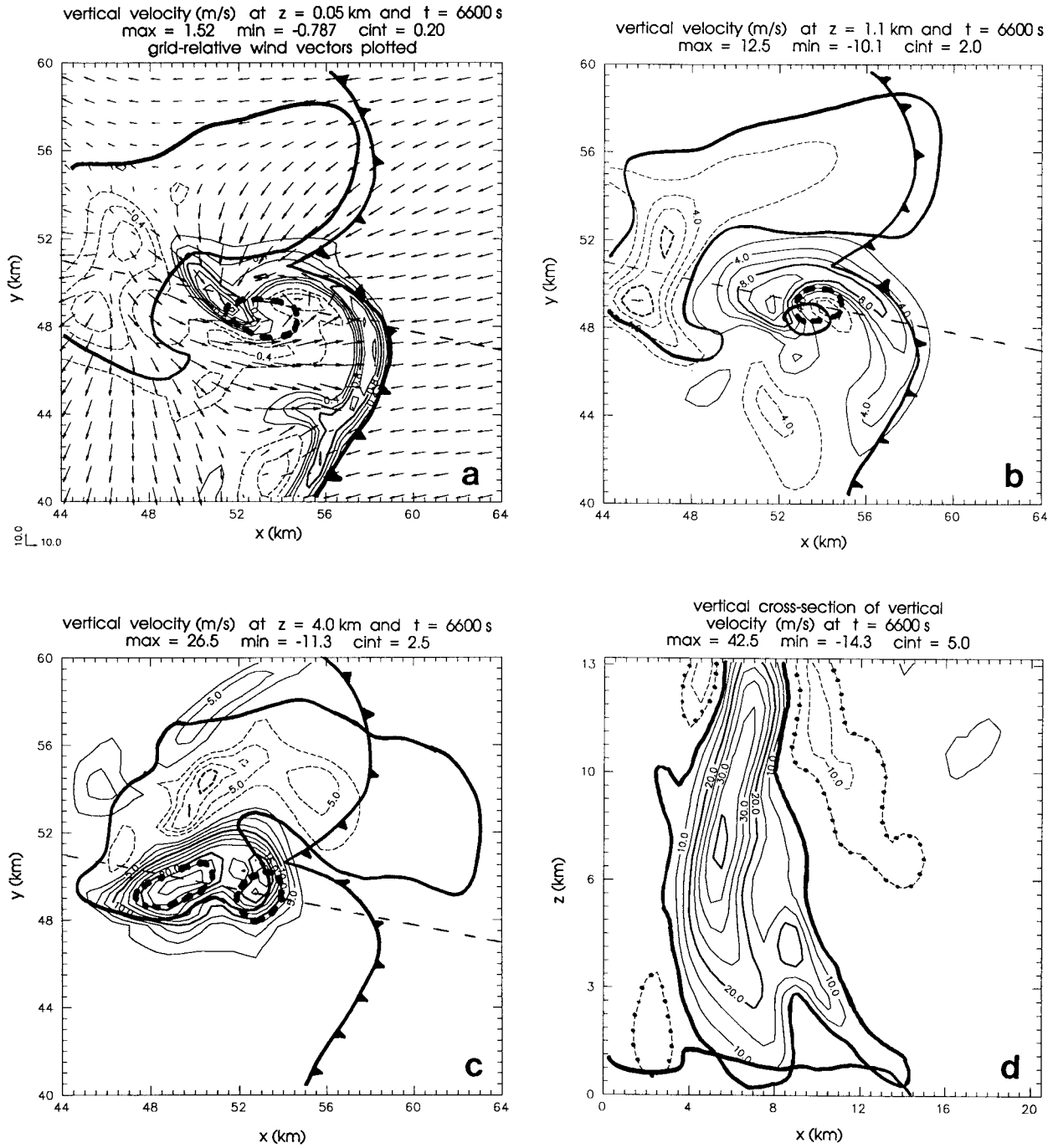

FIG. 20. Same as in Figs. 17a–d except for $t = 6600$ s.

of the occlusion downdraft at the surface and the subsequent development of the third updraft pulse. Near the ground, the convergence term increases to 108 $\times$ 10^{-5} s^{-2}. The tilting term (Fig. 15) also shows significant increases between 6600 and 7000 s, with values rising to 15 $\times$ 10^{-5} s^{-2} just above the surface. Above 1 km, tilting and vertical advection (not shown) become the dominant mechanisms for sudden mesocyclone strengthening.

It has been proposed (e.g., Davies-Jones 1982; Rasmussen and Straka 1996) that the rear-flank/occlusion downdraft plays a role in the transport of vertical vorticity to the ground since its appearance often precedes tornadogenesis. In order to test this hypothesis, a tra-

jectory analysis similar to that discussed in previous sections was undertaken. A square group of parcels centered on the occlusion downdraft at 150 m was integrated backward for 900 s starting at $t = 6600$ s. Similar to the previous analysis, parcels that pass through the occlusion downdraft at low levels appear to have two source regions: the RFD and east of the gust front (Fig. 21a). Two representative parcel trajectories are shown in Figs. 21b,c (i.e., each trajectory shows similar motions to those from the same source region). These are nearly identical to those previously discussed (Figs. 9b and 12b), except that at the end of the trajectory, the parcels rotate around the near-ground mesocyclone into the occlusion downdraft and subsequently descend while their vertical vorticity decreases. In both cases, this decrease results from negative tilting and convergence (not shown), as one would expect for parcels descending into a localized area of divergence. However, the parcels still contain significant cyclonic vorticity and therefore have the potential to spin rapidly once they exit the downdraft and enter the updraft where they can be vertically stretched. Therefore, it appears that the occlusion downdraft may be important for further near-ground vortex intensification by both transporting parcels with significant vertical vorticities to low levels and by increasing surface convergence and subsequent vertical stretching.

e. Stage 4: Mesocyclone/updraft decay and subsequent downshear development

After the occlusion downdraft reaches the surface (6600 s), vertical vorticity in the lowest 4 km peaks between $t = 6700$ and 7200 s (Fig. 7). Dynamically induced downward vertical pressure-gradient forces (not shown) increase from 0.05 to 0.2 m s^{-2} in the lowest kilometer. As the occlusion downdraft (which has merged with the RFD by this time) continues to be driven by this effect, the strong mesocyclone circulation advects the downdraft around the mesocyclone. By 7200 s, the downdraft air wraps completely around the near-ground updraft–mesocyclone, severing the updraft from its inflow. A horizontal cross section at $z = 50$ m (Fig. 22a) shows that the near-ground updraft ($x = 50$ km, $y = 50$ km) has completely separated from the updraft at the gust front and has become enveloped in precipitation. This feature is also apparent at $z = 1$ km (Fig. 22b). The two-celled updraft structure remains intact throughout this period (Fig. 22c), with the downshear portion becoming much larger below 4 km (Fig. 22d).

Once the near-ground mesocyclone completely occludes at 7200 s, near-ground vertical vorticity rapidly decreases (Fig. 7). Inflow of conditionally unstable air into the original updraft is cut off and the updraft becomes embedded in an area of precipitation and surface divergence. As a result, the near-ground mesocyclone completely decays in approximately 15 min. Between $t = 7200$ and 8100 s, stretching of vertical vorticity

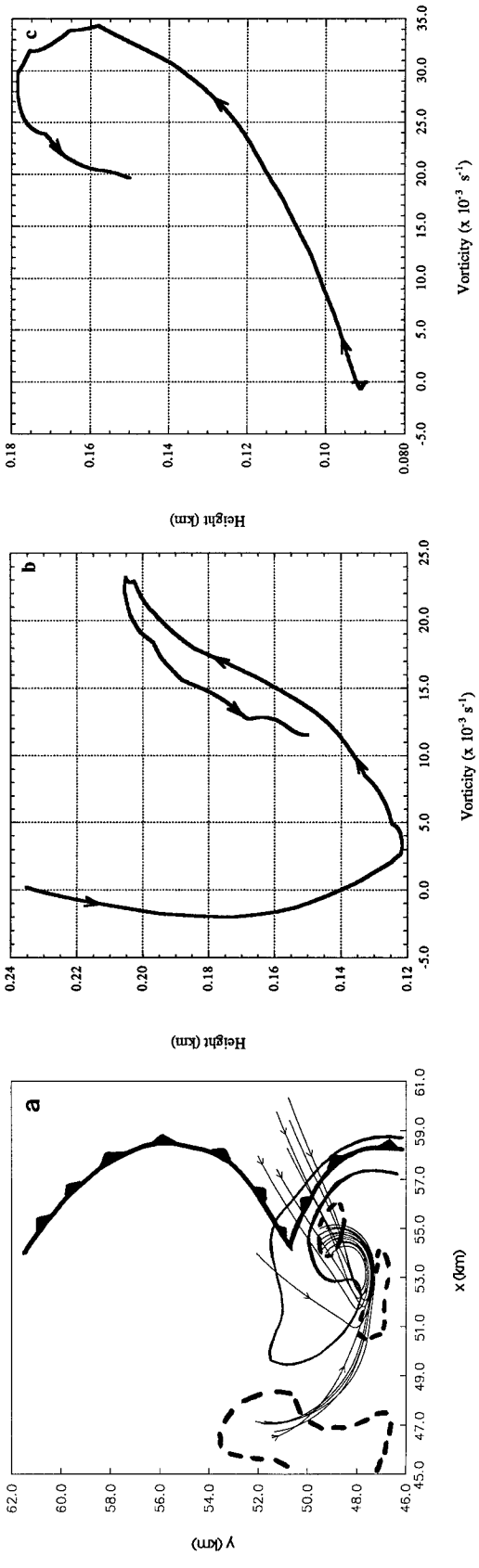

FIG. 21. (a) Same as in Fig. 8a but with the projection of three-dimensional backward trajectories toward the occlusion downdraft indicated. Parcels were started from $z = 150$ m and integrated from $t = 6600$ to 5700 s. Parcels were initially spaced 500 m apart. (b) Vorticity ($\times 10^{-3}$ s^{-1}) vs height (km) plot of a parcel in (a) that originated in the RFD area ($x = 55.0$ km, $y = 49.5$ km). (c) Vorticity ($\times 10^{-3}$ s^{-1}) vs height (km) plot of a parcel in (a) that originated east of the gust front ($x = 54.0$ km, $y = 49.0$ km).

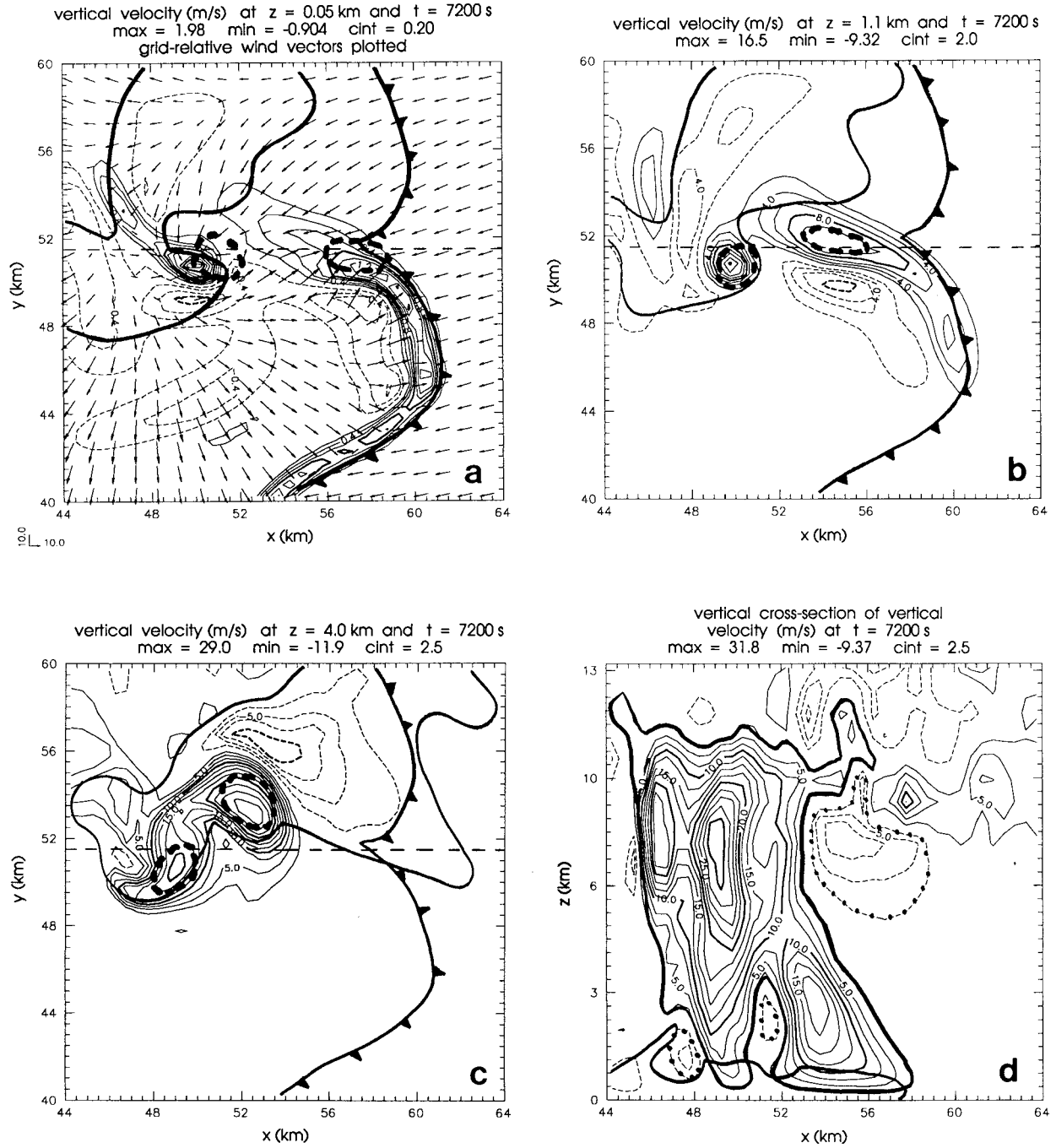

FIG. 22. Same as in Figs. 17a–d except for $t = 7200$ s.

(Fig. 16) decreases from approximately 100×10^{-5} to 12×10^{-5} m s^{-2}. Just above the surface, tilting (Fig. 15) also decreases from 27×10^{-5} to 6×10^{-5} m s^{-2}. An area of unusually strong tilting between $z = 250$ m and 1 km develops nearly simultaneously with the occlusion at 7200 s and lasts for approximately 500 s. This localized maximum occurs when the downdraft first separates the near-ground updraft from the gust front. Horizontal vorticity associated with the updraft–downdraft interface along the gust front is suddenly tilted upward as the occlusion develops. Although this has little effect at the lowest level, it does appear to slightly delay the mesocyclone's decay near $z = 1$ km (Fig. 7).

Following the occlusion, the western (upshear) portion of the updraft begins to weaken since it no longer has potentially buoyant air feeding into it. The eastern

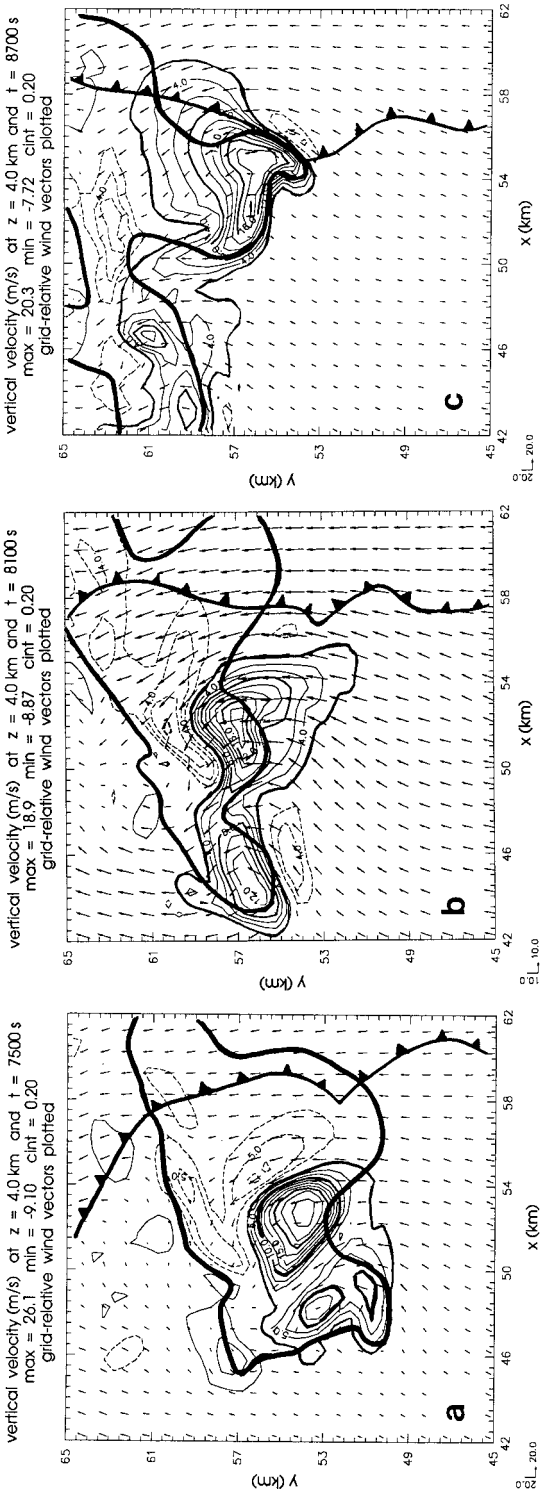

FIG. 23. Horizontal cross sections of vertical velocity at 4 km at (a) $t = 7500$ s, (b) $t = 8100$ s, and (c) $t = 8700$ s. Isoline of 1 g kg^{-1} rainwater mixing ratio indicated by heavy dark line. Contour interval is 2.5, 2.0, and 2.0 m s^{-1}, respectively. Surface cold-pool boundary and wind vectors indicated.

portion of the updraft continues to propagate continuously eastward with the gust front. Figure 23 shows three horizontal sections across the updrafts at 4 km during this transitional period. At $t = 7500$ s, the maximum vertical velocity in the decaying updraft is 15 m s^{-1}. As this updraft and its associated mesocyclone move off to the northwest with the mean flow, its maximum vertical velocity weakens quickly to 10 m s^{-1} by $t = 8700$ s. The new updraft also weakens slightly during the beginning of the transitional period but begins to intensify once it becomes centered over the gust front at $t = 8700$ s.

Figure 17 shows that throughout the period between $t = 7200$ and 9000 s, midlevel vertical vorticity associated with the new updraft remains well above the mesocyclone threshold (>0.01 s^{-1}). In contrast, vertical vorticity below 2 km remains under this threshold for approximately 15 min. After $t = 9000$ s, the new updraft completely separates from the decaying updraft and begins to increase steadily in strength (Fig. 6) without any indication of surface-based updraft pulses.

f. Stage 5: Reintensification of the downshear updraft and new near-ground mesocyclogenesis

During the transitional period described above, the occluded supercell once again begins to reorganize. The continuous nature of the transition has important implications for the next cycle in near-ground mesocyclogenesis. At the surface, the cold pool and gust front have not moved far during the transition (Fig. 24). As the RFD and associated surface outflow decrease in conjunction with the decay of the old updraft, the gust front retrogrades slightly to the west (with the mean surface flow) and takes on a more north–south orientation between $t = 7500$ and 8700 s. Since the cold pool and associated buoyancy contours are still oriented nearly north–south (as in the initial near-ground mesocyclogenesis), baroclinic generation along parcel trajectories may proceed in a similar manner as before without delay.

Figure 24 displays contours of the surface streamwise baroclinic horizontal vorticity generation as defined in (3). As the new updraft moves away from the old occluded updraft and toward the gust front, the area of strongest streamwise baroclinic generation is advected with it. The buoyancy contours and horizontal-vorticity vectors are still oriented primarily north–south. As the new updraft becomes established and inflow increases, the streamwise baroclinic generation term increases from 7×10^{-5} to 15×10^{-5} s^{-2}. The previous occlusion has effectively set the stage for the next cycle of near-ground mesocyclogenesis.

Figure 25 depicts storm structure at $t = 9300$ s. At this time, near-ground mesocyclogenesis of the second cycle has just begun, with the buoyancy contours in the same relative position as during the first cycle. The cross sections depict a storm that is nearly identical in struc-

ture to the supercell at $t = 5100$ s prior to the occlusion (Fig. 4). In order to compare the process of near-ground mesocyclogenesis before and after the first occlusion, another set of backward trajectories was initiated at $t = 9900$ s (not shown). The same parcel analysis presented in section 4b was carried out, and results were qualitatively similar. Positive vorticity was again found to be generated in downdrafts along the western edge of the mesocyclone.

5. Summary and discussion

A numerical simulation of a classic supercell undergoing multiple mesocyclone occlusions was presented. The cycling process in this case can be logically divided into five steps (Fig. 3) and begins with the initiation of an evaporatively driven rear-flank downdraft. The outflow from this downdraft initiates the first of three updraft pulses, which consequently promote intense vortex stretching near the surface and tilting aloft. The downdraft and its associated diabatic cooling is critically important because it also helps establish the near-ground buoyancy gradients along which strong horizontal vorticity is generated. Parcels entering the mesocyclone originate from both the east (up and over the gust front) and from the west (descending in the RFD). Parcels from the west first gain crosswise vorticity through crosswise baroclinic generation, and then gain streamwise vorticity via the exchange of crosswise vorticity and from intense stretching in the streamwise direction (the latter dominating as the parcel nears the near-ground updraft base). This vorticity is then tilted and stretched, resulting in near-ground mesocyclogenesis. Parcels that travel through the RFD gain positive vertical vorticity throughout the latter part of their descent, consistent with the mechanism proposed by Davies-Jones and Brooks (1993) and suggested in the simulations of Grasso and Cotton (1995).

After initial near-ground mesocyclogenesis, the RFD continues to push the gust front outward, forcing secondary updraft development above the gust front on the eastern side of the original updraft. Convergence at the gust front forced by outflow from the RFD also initiates the second updraft pulse. Near-ground vorticity continues to increase with time and a dynamically induced downward pressure-gradient force becomes established. This helps to initiate the occlusion downdraft that reaches the ground, increases convergence at the gust front again, and initiates the third and final updraft pulse. The increase in near-ground convergence and the associated third updraft pulse promote mesocyclone intensification throughout a significant depth.

The strong near-ground mesocyclone intensification has several consequences. First, intense downdrafts continue to push the gust front outward, forcing further development on the eastern flanks of the updraft. Second, the occlusion downdraft merges with the RFD, and the near-ground mesocyclone separates from the gust

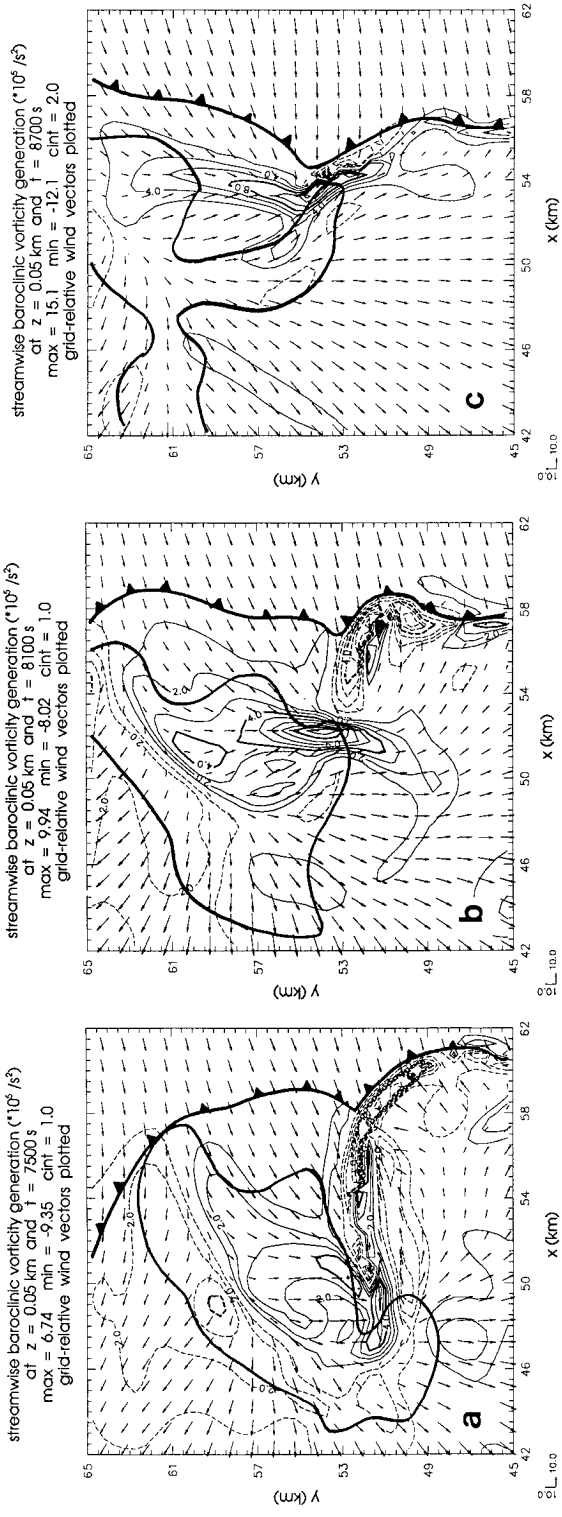

FIG. 24. Horizontal cross sections of the streamwise baroclinic horizontal vorticity generation term at $z = 50$ m at (a) $t = 7500$ s, (b) $t = 8100$ s, and (c) $t = 8700$.s. Isoline of 1 g kg^{-1} rainwater mixing ratio indicated by heavy dark line. Contour intervals are 1.0, 1.0, and 2.0×10^{-5} s^{-2}, respectively. Surface cold-pool boundary and wind vectors indicated.

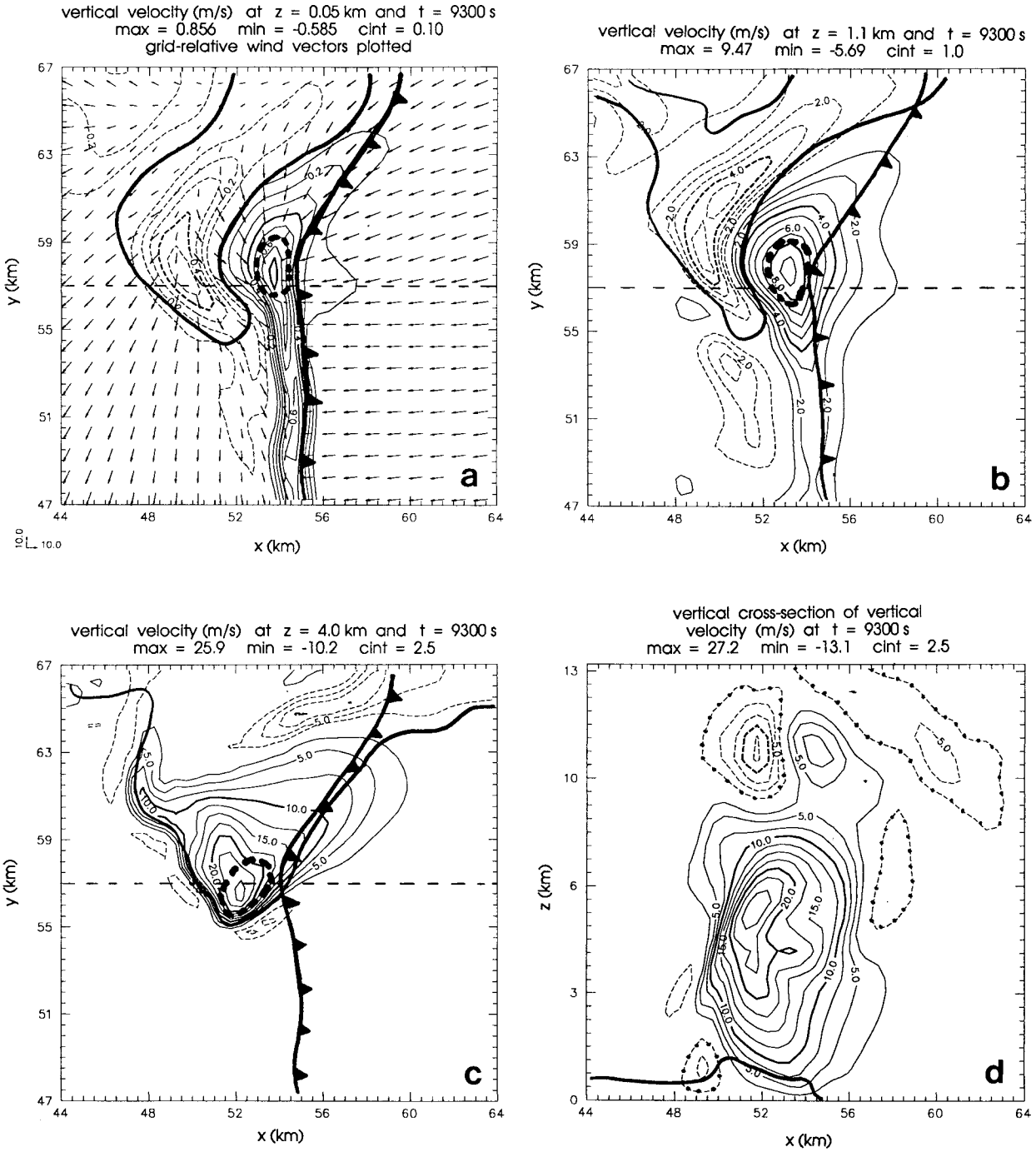

FIG. 25. Same as in Figs. 17a–d except for $t = 9300$. Contour interval is now (a) 0.1 m s^{-1} and (b) 2.0 m s^{-1}.

front and becomes embedded in precipitation. As the old updraft and associated near-ground mesocyclone lose their source of buoyant air, they weaken. This occlusion signals the end of one ''cycle.'' The gust front then advances farther eastward, updraft development on the eastern flank becomes prominent, and the two updrafts finally separate. The new updraft is located over the gust front, and near-ground mesocyclogenesis is once again initiated via the *same* mechanisms as in the first cycle. The presence of a residual cold pool provides ideally oriented buoyancy gradients for the reoccurrence of baroclinic generation effects.

Klemp and Rotunno (1983) present a 6-min nested high-resolution (Δx, Δy = 250 m) simulation of the occlusion process (also using the Del City sounding), which roughly corresponds to our simulation interval

of 6300–6600 s. Similar to the above results, they describe the development of a occluding low-level updraft, a dynamically driven occlusion downdraft, and a secondary updraft maximum along the gust front driven by increased low-level convergence associated with the occlusion. They also suggest that the intensification of low-level vorticity is a result of the tilting of baroclinically generated horizontal vorticity, which is then greatly amplified by strong low-level convergence induced by the occlusion process. Although no trajectory analysis is performed and their vertical resolution is much coarser ($\Delta z = 500$ m), this appears consistent with our results.

The sequence of events in our present simulation, except for the baroclinic generation of horizontal vorticity, also appears consistent with the conceptual models proposed by Lemon and Doswell (1979) and Burgess et al. (1982). However, secondary mesocyclone development is somewhat slower than that described in the observational survey by Burgess et al. (1982). In order to completely understand the cyclic storm problem, it is apparent that further work needs to be undertaken. Observational datasets covering the full occlusion process would be invaluable. Numerical simulations such as the one described here may benefit from increased resolution, realistic interactions of the flow with the ground, and the incorporation of full ice microphysics.

In light of these limitations, further numerical studies are planned that extend this work in two directions: 1) an investigation into the factors that control the structure and periodicity of the cycling, and that delineate between cyclic versus noncyclic storms; and 2) a downscale extension of the problem to cyclic tornadogenesis. We hope that such research may eventually be utilized by the forecast community for the operational prediction of cyclic supercells and tornadoes.

Acknowledgments. The numerical simulations were carried out on the Environmental Computing Application System (ECAS) Cray J90 at the University of Oklahoma. The ECAS is funded by the University of Oklahoma and the NSF under Grant EAR95-1245. Preliminary simulations were carried out on the Cray C90 and Cray T3D at the Pittsburgh Supercomputing Center. Dr. Dan Weber provided the initial version of the trajectory code, and Dr. Rodger Brown and Mr. Vincent Wood provided background information on cyclic storm cases. Dr. D. Lilly provided helpful comments on the manuscript. Some of the graphics were generated using the ZXPLOT package developed by Dr. Ming Xue at the University of Oklahoma. Support for this work was provided by the NSF through Grant ATM92-22576 to the second author, and by Grant ATM91-20009 to the Center for Analysis and Prediction of Storms.

REFERENCES

Agee, E. M., J. T. Snow, and P. Clare, 1976: Multiple vortex features in the tornado cyclone and the occurrence of tornado families. *Mon. Wea. Rev.,* **104,** 552–563.

Brandes, E. A., 1984: Vertical vorticity generation and mesocyclone sustenance in tornadic thunderstorms: The observational evidence. *Mon. Wea. Rev.,* **112,** 2253–2269.

——, 1993: Tornadic thunderstorm characteristics determined with Doppler radar. *The Tornado: Its Structure, Dynamics, Prediction, and Hazards, Geophys. Monogr.,* No. 79, Amer. Geophys. Union, 143–159.

Brooks, H. E., C. A. Doswell III, and R. P. Davies-Jones, 1993: Environmental helicity and the maintenance and evolution of low-level mesocyclones. *The Tornado: Its Structure, Dynamics, Prediction, and Hazards, Geophys. Monogr.,* No. 79, Amer. Geophys. Union, 97–104.

——, ——, and R. B. Wilhelmson, 1994: On the role of midtropospheric winds in the evolution and maintenance of low-level mesocyclones. *Mon. Wea. Rev.,* **122,** 126–136.

Burgess, D. W., V. T. Wood, and R. A. Brown, 1982: Mesocyclone evolution statistics. Preprints, *12th Conf. on Severe Local Storms,* San Antonio, TX, Amer. Meteor. Soc., 422–424.

Darkow, G. L., and J. C. Roos, 1970: Multiple tornado producing thunderstorms and their apparent cyclic variations in intensity. Preprints, *14th Conf. on Radar Meteorology,* Tucson, AZ, Amer. Meteor. Soc., 305–308.

Davies-Jones, R., 1982: Observational and theoretical aspects of tornadogenesis. *Intense Atmospheric Vortices,* L. Bengtsson and J. Lighthill, Eds., Springer-Verlag, 175–189.

——, 1984: Streamwise vorticity: The origin of updraft rotation in supercell storms. *J. Atmos. Sci.,* **41,** 2991–3006.

——, 1996: Formulas for the barotropic and baroclinic components of vorticity with applications to vortex formation near the ground. Preprints, *Seventh Conf. on Mesoscale Processes,* Reading, United Kingdom, Amer. Meteor. Soc., 14–16.

——, and H. E. Brooks, 1993: Mesocyclogenesis from a theoretical perspective. *The Tornado: Its Structure, Dynamics, Prediction, and Hazards, Geophys. Monogr.,* No. 79, Amer. Geophys. Union, 105–114.

——, D. Burgess, and M. Foster, 1990: Test of helicity as a tornado forecast parameter. Preprints, *16th Conf. on Severe Local Storms,* Kananaskis Park, Alberta, Canada, Amer. Meteor. Soc., 588–592.

Doswell, C. A. III, and D. W. Burgess, 1993: Tornadoes and tornadic storms: A review of conceptual models. *The Tornado: Its Structure, Dynamics, Prediction, and Hazards, Geophys. Monogr.,* No. 79, Amer. Geophys. Union, 161–172.

Dowell, D. C., H. B. Bluestein, and D. P. Jorgensen, 1997: Airborne Doppler radar analysis of supercells during COPS-91. *Mon. Wea. Rev.,* **125,** 365–383.

Droegemeier, K. K., S. M. Lazarus, and R. Davies-Jones, 1993: The influence of helicity on numerically simulated convective storms. *Mon. Wea. Rev.,* **121,** 2005–2029.

Foote, G. B., and H. W. Frank, 1983: Case study of a hailstorm in Colorado. Part III: Airflow from triple-Doppler measurements. *J. Atmos. Sci.,* **40,** 686–707.

Forbes, G. S., 1975: Relationship between tornadoes and hook echoes associated with left-turn tornado families. Preprints, *Ninth Conf. on Severe Local Storms,* Norman, OK, Amer. Meteor. Soc., 280–285.

——, 1977: Thunderstorm-scale variations of echoes associated with left-turn tornado families. Preprints, *10th Conf. on Severe Local Storms,* Omaha, NE, Amer. Meteor. Soc., 321–326.

Foster, M. P., A. R. Moller, L. J. Wicker, and L. Cantrell, 1994: The rapid evolution of a tornadic small supercell: Observations and simulation. Preprints, *14th Conf. on Weather Analysis and Forecasting,* Dallas, TX, Amer. Meteor. Soc., 323–328.

Fujita, T. T., 1975: New evidence from April 3–4, 1974 Tornadoes. Preprints, *Ninth Conf. on Severe Local Storms,* Norman, OK, Amer. Meteor. Soc., 248–255.

——, D. L. Bradbury, and C. F. Van Thullenar, 1970: Palm Sunday tornadoes of April 11, 1965. *Mon. Wea. Rev.,* **98,** 29–69.

Grasso, L. D., and W. R. Cotton, 1995: Numerical simulation of a tornado vortex. *J. Atmos. Sci.,* **52,** 1192–1203.

Hoecker, W. H., 1959: History and measurement of two major Scottsbluff tornadoes of 27 June 1955. *Bull. Amer. Meteor. Soc.,* **40,** 117–133.

Jensen, B., E. N. Rasmussen, T. P. Marshall, and M. A. Mabey, 1983: Storm scale structure of the Pampa storm. Preprints, *13th Conf. on Severe Local Storms,* Tulsa, OK, Amer. Meteor. Soc., 85–88.

Johnson, K. W., P. S. Ray, B. C. Johnson, and R. P. Davies-Jones, 1987: Observations related to the rotational dynamics of the 20 May 1977 tornadic storms. *Mon. Wea. Rev.,* **115,** 2463–2478.

Klemp, J. B., and R. Rotunno, 1983: A study of the tornadic region within a supercell thunderstorm. *J. Atmos. Sci.,* **40,** 359–377.

——, R. B. Wilhelmson, and P. S. Ray, 1981: Observed and numerically simulated structure of a mature supercell thunderstorm. *J. Atmos. Sci.,* **38,** 1558–1580.

Knupp, K. R., 1987: Downdrafts within precipitating high plains cumulonimbi. Part I: General kinematic structure. *J. Atmos. Sci.,* **44,** 987–1008.

Kulie, M. S., and Y. Lin, 1998: The structure and evolution of a numerically simulated high-precipitation supercell thunderstorm. *Mon. Wea. Rev.,* **126,** 2090–2116.

Lemon, L. R., and C. A. Doswell III, 1979: Severe thunderstorm evolution and mesocyclone structure as related to tornadogenesis. *Mon. Wea. Rev.,* **107,** 1184–1197.

Leslie, L. M., 1971: The development of concentrated vortices: A numerical study. *J. Fluid Mech.,* **48,** 1–21.

Lilly, D. K., 1982: The development and maintenance of rotation in convective storms. *Intense Atmospheric Vortices,* L. Bengtsson and J. Lighthill, Eds., Springer-Verlag, 149–160.

——, 1983: Dynamics of rotating thunderstorms. *Mesoscale Meteorology: Theories, Observations and Models,* D. K. Lilly and T. Gal-Chen, Eds., Reidel, 531–544.

——, 1986a: The structure, energetics, and propagation of rotating convective storms. Part I: Energy exchange with the mean flow. *J. Atmos. Sci.,* **43,** 113–125.

——, 1986b: The structure, energetics, and propagation of rotating convective storms. Part II: Helicity and storm stabilization. *J. Atmos. Sci.,* **43,** 126–140.

McCaul, E. W., Jr., 1991: Buoyancy and shear characteristics of hurricane tornado environments. *Mon. Wea. Rev.,* **119,** 1954–1978.

——, 1993: Observations and simulations of hurricane-spawned tornadic storms. *The Tornado: Its Structure, Dynamics, Prediction, and Hazards, Geophys. Monogr.,* No. 79, Amer. Geophys. Union, 119–142.

——, and M. L. Weisman, 1996: Simulations of shallow supercell storms in landfalling hurricane environments. *Mon. Wea. Rev.,* **124,** 408–429.

Moller, A. R., C. A. Doswell III, M. P. Foster, and G. R. Woodall, 1994: The operational recognition of supercell thunderstorm environments and storm structures. *Wea. Forecasting,* **9,** 327–347.

Monteverdi, J. P., and J. Quadros, 1994: Convective and rotational parameters associated with three tornado episodes in northern and central California. *Wea. Forecasting,* **9,** 285–300.

Nelson, S. P., 1987: The hybrid multicellular–supercellular storm—An efficient hail producer. Part II: General characteristics and implications for hail growth. *J. Atmos. Sci.,* **44,** 2060–2073.

Rasmussen, E. N., and J. M. Straka, 1996: Mobile mesonet observations of tornadoes during VORTEX-95. Preprints, *18th Conf. on Severe Local Storms,* San Francisco, CA, Amer. Meteor. Soc., 1–5.

——, R. E. Peterson, J. E. Minor, and B. D. Campbell, 1982: Evolutionary characteristics and photogrammetric determination of wind speeds within the Tulia outbreak tornadoes 28 May 1980. Preprints, *12th Conf. on Severe Local Storms,* San Antonio, TX, Amer. Meteor. Soc., 301–304.

Ray, P. S., B. C. Johnson, K. W. Johnson, J. S. Bradberry, J. J. Stephens, K. K. Wagner, R. B. Wilhelmson, and J. B. Klemp, 1981: The morphology of several tornadic storms on 20 May 1977. *J. Atmos. Sci.,* **38,** 1643–1663.

Richardson, Y. P., and K. K. Droegemeier, 1996: An investigation of the dynamics governing organized multicell rotation and transition. Preprints, *18th Conf. on Severe Local Storms,* San Francisco, CA, Amer. Meteor. Soc., 195–199.

——, K. K. Droegemeier, and R. Davies-Jones, 1998: A study of the influence of horizontally varying vertical shear and CAPE on numerically simulated convective storms. Preprints, *19th Conf. on Severe Local Storms,* Minneapolis, MN, Amer. Meteor. Soc., 249–252.

Rotunno, R., and J. B. Klemp, 1982: The influence of the shear-induced pressure gradient on thunderstorm motion. *Mon. Wea. Rev.,* **110,** 136–151.

——, and ——, 1985: On the rotation and propagation of numerically simulated supercell thunderstorms. *J. Atmos. Sci.,* **42,** 271–292.

Scorer, R. S., 1978: *Environmental Aerodynamics.* Ellis Horwood, 488 pp.

Simpson, J. E., 1972: The effect of the lower boundary on the head of a gravity current. *J. Fluid Mech.,* **53,** 759–768.

Snow, J. T., and E. M. Agee, 1975: Vortex splitting in the mesocyclone and the occurrence of tornado families. Preprints, *Ninth Conf. on Severe Local Storms,* Norman, OK, Amer. Meteor. Soc., 270–277.

Trapp, R. J., and R. Davies-Jones, 1997: Tornadogenesis with and without a dynamic pipe effect. *J. Atmos. Sci.,* **54,** 113–133.

Vasiloff, S. V., E. A. Brandes, R. P. Davies-Jones, and P. S. Ray, 1986: An investigation of the transition from multicell to supercell storms. *J. Climate Appl. Meteor.,* **25,** 1022–1036.

Weisman, M. L., and J. B. Klemp, 1982: The dependence of numerically simulated convective storms on vertical wind shear and buoyancy. *Mon. Wea. Rev.,* **110,** 504–520.

Wicker, L. J., and R. B. Wilhelmson, 1995: Simulation and analysis of tornado development and decay within a three-dimensional supercell thunderstorm. *J. Atmos. Sci.,* **52,** 2675–2703.

——, and L. Cantrell, 1996: The role of vertical buoyancy distribution in miniature supercells. Preprints, *18th Conf. on Severe Local Storms,* San Francisco, CA, Amer. Meteor. Soc., 225–229.

Xue, M., K. K. Droegemeier, V. Wong, A. Shapiro, and K. Brewster, 1995: ARPS Version 4.0 User's Guide. Center for Analysis and Prediction of Storms, University of Oklahoma, 380 pp. [Available from Center for Analysis and Prediction of Storms, University of Oklahoma, Norman, OK 73019-1011.]